Accepted to Phys. Fluids 10.1063/5.0101738

Stimuli-responsive polyelectrolyte brushes for regulating streaming current magnetic field and energy conversion efficiency in soft nanopores

Morteza Sadeghi,[1, a)] Mohammad Hassan Saidi,[1, b)] Martin Kröger,[2, c)] and Mario Tagliazucchi[3, d)]
[1)]*Center of Excellence in Energy Conversion (CEEC), School of Mechanical Engineering, Sharif University of Technology, Tehran 11155-9567, Iran.*
[2)]*Polymer Physics, Department of Materials, ETH Zurich, CH-8093 Zurich, Switzerland.*
[3)]*Universidad de Buenos Aires, Facultad de Ciencias Exactas y Naturales, Departamento de Química Inorgánica Analítica y Química Física, Buenos Aires, Argentina.*

The electrokinetic energy conversion, electroviscous effect, and induced internal and external magnetic fields in a smart polyelectrolyte grafted "soft" nanopore with pH responsiveness are studied here using an efficient molecular theory approach. The analysis is based on writing the total free energy of the system, including the conformational entropy of the flexible, self-avoiding polymer chains and the translational entropy of the mobile species, the electrostatic interactions, and the free energy due to chemical equilibrium reactions. Then the free energy is minimized, while satisfying the necessary constraints to find the equilibrium state of the system. The predictions of the model are shown to be in excellent agreement with analytical solutions derived for special cases. We discuss the effect of different influential environmental and polymer brush parameters in detail and show that the electrokinetic energy conversion efficiency is optimal at moderate pH values and low background salt concentrations. It is also shown that the electrokinetic energy conversion efficiency is a complex function depending on both the environmental and polymer brush properties. Notably, high slip coefficients or high polymer grafting densities do not necessarily lead to a high energy conversion efficiency. Magnetic fields readouts allow to measure streaming currents through nanopores without the need of electrodes, and may be utilized as a secondary electronic signature in nanopore sensing techniques. It is shown that in nanopores modified with polyelectrolyte brushes the induced magnetic fields can be tens of times larger than those in solid-state nanopores having only surface charges. We show that by tuning the pH, background salt concentration, surface charge and polyelectrolyte grafting density, the magnitude of the internal and external magnetic fields can be significantly changed and controlled in a wide range.

I. Introduction

There is a strong interest in the transport properties of nanochannels due to their promising applications in biosensing,[1–4] synthetic gates,[5,6] nanofluidic circuits,[7,8] analyte detection[9,10] and energy conversion.[11,12] The main operation principle of nanopore sensing is analyzing the ionic current of a nanopore during the translocation of an analyte, e.g., DNA, RNA and proteins. One of the major drawbacks in nanopore sensing is the fast translocation of bio-molecules, which makes the readout process difficult.[13] The use of a pressure gradient has been proposed as a possible solution for this issue.[13–16] In this method, the pressure difference causes a counterbalance force slowing down the translocation speed. It has been reported that this procedure can significantly reduce the translocation velocity without deleterious effects on the capture rate or the signal to noise ratio. Using pressure gradients in nanochannels also has another important application in electrokinetic energy conversion.[17–19] In fact, electrokinetic effects can be utilized for direct conversion of electrochemical energy into kinetic energy or vice versa. In the first case, named electroosmosis, a voltage applied between the two ends of the nanopore causes the electrolyte solution to be dragged along with an ionic current and operates as a pump under the influence of a direct (DC) current[20–22] or alternating (AC) current.[23] While in the reverse case, a pressure gradient causes a flux of the solution transferring ions along with it, which induces a streaming potential and current that can be utilized for power generation and electropolymerization.[24] In this operation, the streaming current, similar to electric currents, induces internal and external magnetic fields, which can be used as complementary signals in the readout of label-free nanopore sequencing.[25] The applied pressure gradient can be used not only as a means of slowing down the particle movement but also the induced magnetic field can be used to detect a secondary signal in addition to the ionic current to enhance the efficiency of the readout process in a non-invasively approach. Moreover, magnetic fields provide an unique and novel approach to measure pressure-induced streaming currents through nanopores without the need of external electrodes. Therefore, in this work, we aim to focus on the flows created by applying a pressure gradient between the two ends of the pore for two main purposes: (1) investigating their application as a source of electricity, and (2) studying the internal and external magnetic fields created by these flows and analyzing their application as a supplementary sensing technique. Inspired by nature and by the recent advances in nanofabrication techniques, a new wave of nanochannels and nanopores is born by coating polymer and polyelectrolyte (PE) brushes on interface surfaces. In these systems, the characteristic channel widths are similar to the solution Debye length and the extension of the polymer chains. The resulting competition between different length scales can lead to unique features and applications, especially

[a)]Author to whom correspondence should be addressed: morteza.sadeghi9@gmail.com
[b)]Electronic Email: saman@sharif.edu
[c)]Electronic Email: mk@mat.ethz.ch
[d)]Electronic Email: mario@qi.fcen.uba.ar

when the polymer chains are made from responsive materials. Among those, the transport through solid-state nanopores modified with pH-responsive polyelectrolyte brushes can be easily tuned by controlling the environment properties, like the pH and background salt concentration, which promises major advances in applications such as the manipulation of ion transport,[26] bio-sensing[27] and current rectification.[28]

In this work, we refer to nanochannels that are not coated by polyelectrolyte chains as "solid-state nanopores" or "bare solid-state nanopore", in contrast to the polymer-modified nanopores, which are referred as "soft nanopores". The rectification properties of a conical nanopore functionalized with smart polymer brushes was experimentally investigated by Yameen et al.[29] The responsive brushes were constituted of zwitterionic monomers whose charge was tuned via pH changes in the environmental conditions. The authors showed that this technique can provide a high degree of control over the rectification properties of the nanopore. In a similar experimental investigation,[5] the authors studied the performance of a solid-state nanopore modified with pH-responsive poly(4-vinyl pyridine) brushes and revealed that this nanopore could act as gate-keepers, which manage and constrain the flow of ionic species through the confined environment. Other experimental examples of pH-responsive nanopores include the ionic transport regulation via pH in solid-state nanopores modified with polyprotic polymer brushes[30] and pH-tunable nanofluidic diodes prepared from a protein ion channel reconstituted on a planar phospholipid membrane.[31]

Electrokinetic energy conversion has been initially studied in the 1960's by Osterle and co-workers[32,33] and Burgreen and Nikache.[34,35] Because of the renewed interest in nanopores during the past decade, many other researchers have continued working on this topic.[12,17,36–39] However, the number of investigations considering soft polymer-modified nanochannels is still small[40–44] and most of them have treated the polyelectrolyte chains as a soft layer with a fixed constant thickness[40–43,45] and a fixed surface charge density.[40–42,45] Furthermore, to the best of our knowledge, magnetic fields induced by the streaming potential have not been yet studied in nanopores coated by polymer chains. Therefore, our goal in this article is to fill this gap in the literature by (1) considering pH-regulated polyelectrolyte brushes and modeling them using a more rigorous approach than the ones employed in previous works and (2) advance our understanding of the internal and external magnetic fields induced by pressure-driven streaming current in a pH-regulated polyelectrolyte-grafted nanopore.

Several theoretical studies have been undertaken to study electrokinetic flows inside micro/nanochannels using the mean-field approaches, such as Poisson-Nernst-Planck (PNP)[46–49] and Poisson-Boltzmann (PB)[50,51] and, in a more simplified approach, using the Debye–Hückel approximation.[21,22,52,53] Although these methods make the analysis relatively easy and computationally inexpensive, they do not provide detailed information about the behavior of the PE brushes and do not incorporate molecular details of the system like the polymer conformations, the electric charges, the molecular organization inside the polyelectrolyte layer (PEL), and the sizes of the ions and monomers. The molecular theory we use here to model polyelectrolyte chains is a powerful approach developed by Szleifer and co-workers, which addresses all of these deficiencies and provides a continuum framework to capture the coupling between the physical behavior and the chemical states of the system. This theory has been used in the past to study the morphology and structure of PE-brush modified nanochannels under various environmental conditions[54–56] and for different potential applications.[57–62] The present study aims at utilizing the molecular theory approach, which is considerably less expensive than particle based methods like molecular dynamics (MD) simulations and more detailed than mean-field theories based on the PB approximation. We investigate in this work the electroviscous effects, electrochemical energy conversion, degree of ionization of the weak PE functional groups and the internal and external magnetic fields in nanochannels coated by pH-responsive polyelectrolyte brushes. The theory is generally based on writing the overall free energy of the system and then minimizing it with respect to the functions that describe the structure of the system in order to find its equilibrium state. Moreover, analytical solutions are obtained for some special cases.

FIG. 1. Schematic representation of the problem under consideration. The inner wall is coated with PE chains responsive to the pH and salt concentration of the solution. A pressure difference ΔP is exerted between the two ends (higher pressure at the bottom, $dP/dZ < 0$); R and Z are the radial and axial directions, respectively. $\mathbf{j}^-_{\mathrm{str},P}$, and $\mathbf{j}^-_{\mathrm{str},E}$ denote the streaming flux densities of anions due to the applied pressure gradient and the induced back electroosmotic transport, respectively. $\mathbf{j}^-_{\mathrm{con}}$ is the conduction flux density of the negative ions, and $\mathbf{E}_{\mathrm{str}}$ and $\mathbf{B}$ are the induced streaming and magnetic fields, respectively.

II. Problem formulation

We consider here a layer of pH-responsive polyelectrolyte chains endgrafted to the interior surface of a cylindrical nanopore and immersed in an electrolyte solution containing KCl. The schematic of the problem alongside with the coordinate system is shown in Fig. 1. The nanopore has a radius R_{pore} and a length L_{pore} and connects two reservoirs filled with the electrolyte solution. The system contains N_p polymer chains end-tethered to the inner surface of the nanopore with a total area equal to $A_{\mathrm{pore}} = 2\pi R_{\mathrm{pore}} L_{\mathrm{pore}}$, which results in a surface grafting density $\sigma = N_p/(2\pi R_{\mathrm{pore}} L_{\mathrm{pore}})$. The degree of polymerization of the polymer brushes is N. Each segment in the polyelectrolyte is a weak base, which has a +1 charge at low (acidic) pH and a zero charge at high (basic) pH. We specifically choose a pKa of 5.2 for the segments in order to model a poly(vinylpyridine) brush, such as that used to modify solid-state nanochannels in the past.[5,63] Thus, the acid-base reaction of the monomers is given by:

$$\text{Pol-py}H^+ \longleftrightarrow \text{Pol-py} + H^+ \tag{1}$$

$$K_a = \frac{[\text{Pol-py}][H^+]}{[\text{Pol-py}H^+]} \tag{2}$$

where Pol-py and Pol-pyH$^+$ denote a neutral and protonated pyridine segment, respectively, and K_a is the acid-base equilibrium constant for the deprotonation of the Pol-pyH$^+$ segment (Eq. (1)).[58] It should be noted that in previous derivations of the molecular theory,[63] the acid-base equilibrium of the pyridine was considered in terms of the protonation of the pyridine and thus the expression for K_b was used instead of that of K_a. Both formulations of the theory are of course equivalent and produce the same final result.

It is further assumed that the system is narrow ($R_{\text{pore}} \ll L_{\text{pore}}$) and, due to its axiosymmetric geometry, inhomogeneities will be considered only in the radial direction. The flow inside the pore is generated by a pressure gradient applied between its two ends, which leads to a streaming flux density $\mathbf{j}^-_{\text{str},P}$ due to the fluid motion and transport of the negative ions. Moreover, in the open external circuit (OEC) case the accumulation (depletion) of the negative mobile counter ions in the lower (upper) end of the nanochannel produces a steady-state electric field $\mathbf{E}_{\text{str}} = E_{\text{str}}\mathbf{e}_Z$ in the Z-direction, whose modulus E_{str} is known as streaming potential. This streaming field creates both a conduction flux density of negative ions $\mathbf{j}^-_{\text{con}}$ and an electroosmotic (EO) flow in the opposite direction of the fluid motion inside the pore. The induced EO flow causes a streaming flux density shown here by $\mathbf{j}^-_{\text{str,E}}$. The streaming current I_{str}, and conduction current I_{con}, are the surface integral of the pertinent streaming and conduction flux densities, respectively. It is also noteworthy that for the external short-circuit (ESC) case, where there is no induced electrical field, we have only $\mathbf{j}^-_{\text{str},P}$. For simplicity the subscript P is omitted for this case in the rest of manuscript.

The structure of the system is obtained with a molecular theory, which is based on a single chain mean-field approximation. The fundamental idea is to obtain the equilibrium condition of the system by minimizing its total free energy. In the derivation of the present form of the molecular theory, several assumptions are made that should to be pointed out first. Firstly, the molecular theory predicts the molecular organization of the system in equilibrium. We assume here that the equilibrium structure of the system is still valid in the steady state and use it to calculate ion fluxes with the Nernst-Planck equation. This approximation will be good for small external perturbations (low applied pressures). The mean-field nature of the theory is also an important approximation as it neglects correlations, which would affect for example the activity coefficients of the ions. Although this approach has some limitations, it has many advantages to model large systems that would be very expensive (if not impossible[64]) to study with particle-based approaches such as MD[58] if it is not possible. The molecular theory incorporates many molecular details of the system and provides us with information at the nano/micro scale that cannot be captured using continuum approaches, such as Poisson-Boltzmann and PNP. It should be noted that the PNP approach can be thought as a limiting case of the non-equilibrium molecular theory for the case where (1) there are no polymer chains in the system, (2) there is no chemical equilibria, and (3) there are no steric (excluded volume) repulsions.[65]

The first step in the derivation of the theory is to write the total Helmholtz free energy functional (F) of the system,

$$\frac{\beta F}{A_{\text{pore}}} = \sigma \sum_{\alpha} P(\alpha) \ln P(\alpha) + \int_0^{R_{\text{pore}}} G(R) w(R) dR + \beta \sigma_s \Psi(R_{\text{pore}}) \tag{3}$$

where $\beta = 1/k_{\text{B}}T$, k_{B} is the Boltzmann constant and T is temperature. The first term in Eq. (3) is the entropy arising from different polymer chain conformations, where $P(\alpha)$ is the, yet unknown, probability of finding a polymer chain in conformation α and the sum runs over all possible conformations. σ is the surface coverage of the polyelectrolyte chains. The second term includes the radial free energy densities due to three different modes of contributions, $w(R) = w_{\text{trans}}(R) + w_{\text{react}}(R) + w_{\text{electro}}(R)$, where R denotes the distance to the axis of the pore and $G(R)$ is a factor that accounts for the curvature effect of the cylindrical nanopore defined as $G(R) = A(R)/A_{\text{pore}} = R/R_{\text{pore}}$. The term $w_{\text{trans}}(R)$ represents the contribution from the translational entropies of all mobile species, given by

$$w_{\text{trans}}(R) = \rho_w(R)\{\ln[\rho_w(R)v_w] - 1\} + \sum_{i\in\text{ions}} \rho_i(R)\{\ln[\rho_i(R)v_w] - 1\} \tag{4}$$

where $\rho_i(R)$ denotes the number density of species i at radial position R, v_w stands for the volume of a water molecule and subscript 'ions' represent all mobile ion species including K^+, Cl^-, H^+, and OH^-. The second contribution $w_{\text{react}}(R)$ is the free energy density due to the acid-base equilibrium reactions calculated as

$$\begin{aligned} w_{\text{react}}(R) = {} & \langle\rho_p(R)\rangle\{f(R)\ln f(R) + [1-f(R)]\ln[1-f(R)]\} \\ & + \langle\rho_p(R)\rangle\left\{\beta\mu^0_{\text{PyH}^+} f(R) + \beta\mu^0_{\text{Py}}[1-f(R)]\right\} \\ & + \beta\mu^0_{\text{OH}^-}\rho_{\text{OH}^-}(R) + \beta\mu^0_{\text{H}^+}\rho_{\text{H}^+}(R) \end{aligned} \tag{5}$$

where $\langle\rho_p(R)\rangle = \sigma\sum_\alpha P(\alpha)n_\alpha(R)/G(R)$ is the average radial polymer number density, $n_\alpha(R)dR$ is the number of monomers residing between R and $R+dR$ for a chain in conformation α, μ^0_i is the standard chemical potential of species i, and

$$f(R) = \frac{[\text{Pol-pyH}^+(R)]}{[\text{Pol-pyH}^+(R)] + [\text{Pol-py}(R)]} \tag{6}$$

is the degree of ionization of the monomers at radius R. The third term contributing to the free energy functional is $w_{\text{electro}}(R)$, which accounts for the electrostatic interactions,

$$w_{\text{electro}}(R) = \beta\left\{\langle\rho_q(R)\rangle\Psi(R) - \frac{1}{2}\varepsilon_f[\nabla_R\Psi(R)]^2\right\} \tag{7}$$

Here, $\Psi(R)$ is the electrical potential field, ε_f is the permittivity of the solution (which we assumed to be constant through the system), ∇_R stands for the gradient in the R-direction and $\langle\rho_q(R)\rangle = q_p f(R)\langle\rho_p(R)\rangle + \sum_{i\in\text{ions}} q_i\rho_i(R)$ is the average density of electrical charges at radial location R. In this relation, q_p and q_i are the electrical charges of a protonated monomer and the ionic species i, respectively. In Eq. (3), the third term is the free energy due to the surface charge density σ_s of the pore.

We consider a good solvent quality, thus there are not net short-range nonelectrostatic attractions between the monomers of the polymer and between a monomer and the solvent. The repulsive intramolecular and intermolecular interactions are taken into account through assuming a hard core potential and are enforced through the generation of self-avoiding polymer conformations for intramolecular monomer-monomer interactions, and by using a volume-filling (packing) constraint for the other repulsive interactions. The volume filling constraint is written as

$$\langle \phi_p(R)\rangle + \sum_{i\in\{\text{ions},w\}} \phi_i(R) = 1 \tag{8}$$

where $\phi_i(R) = \rho_i(R)v_i$ and $\langle\phi_p(R)\rangle = \langle\rho_p(R)\rangle v_p$ are the volume fractions of mobile species i (with volume v_i) and polymer monomers (with volume v_p) at position R, respectively. The normalization of probability distribution function of the conformations of the polymer, $\sum_\alpha P(\alpha) = 1$, is a second constraint that should be enforced. Finally, since we are dealing with equilibrium conditions, the chemical potentials of the ions are fixed to those inside the reservoirs. Therefore, the proper thermodynamic potential that should be considered is not the Helmholtz free of the system, F, but rather its Legrendre transform, $F - \sum_{i\in\text{ions}}\mu_i n_i$. Considering this Legrendre transform and introducing the constraints through Lagrange multipliers, results in:

$$\begin{aligned}\frac{\beta\Omega}{A_{\text{pore}}} = \frac{\beta F}{A_{\text{pore}}} &- \beta\sum_{i\in\text{ions}}\mu_i\int G(R)\rho_i(R)dR \\ &-\beta\mu_{\text{H}^+}\int G(R)f(R)\langle\rho_p(R)\rangle dR - \chi\left[1-\sum_\alpha P(\alpha)\right] \\ &+\beta\int G(R)\pi(R)\left[\langle\phi_p(R)\rangle - 1 + \sum_i \phi_i(R)\right]dR\end{aligned} \tag{9}$$

where $\pi(R)$ and χ are Lagrange multipliers corresponding to the incompressibility and normalization constraints, respectively. In fact, the Lagrange multiplier $\pi(R)$, which enforces the packing constraint, is a position-dependent osmotic pressure. Note also that the third term in the RHS accounts for the $-\mu_i n_i$ term of those protons that are bound to monomer segments. To obtain the equilibrium condition of the system, the functional Ω defined by Eq. (9) should be extremized with respect to the unknown structural functions. To do so, it is convenient to introduce a number of dimensionless parameters:

$$\begin{aligned}&r = \frac{R}{R_{\text{pore}}}, \qquad \pi^* = \beta\pi v_w, \qquad q^* = \frac{q}{e}, \qquad v^* = \frac{v}{v_w}, \\ &\psi = \beta e\Psi, \qquad \lambda = \left(\frac{\beta e^2}{\varepsilon_f v_w}\right)^{-1/2}, \quad \omega = \frac{R_{\text{pore}}}{\lambda}\end{aligned} \tag{10}$$

With the help of these dimensionless variables, the functional Ω is an extreme, if the following dimensionless equations hold for $i \in \{\text{ions}\}$

$$\phi_i(r) = \phi_i^{\text{bulk}}\exp\left\{-\left[\pi^*(r) - \pi^{*,\text{bulk}}\right]v_i^* - q_i^*\psi(r)\right\}, \tag{11}$$

$$\phi_w(r) = \exp[-\pi^*(r)], \tag{12}$$

$$\frac{f(r)}{1-f(r)} = \frac{\phi_{\text{H}^+}(r)\exp[\pi^*(r)v_{\text{H}^+}^*]}{K_a N_A v_{\text{H}^+}}, \tag{13}$$

$$P(\alpha) = \frac{1}{¶}\exp\int -n_\alpha(r)\left[\ln f(r) + q_p^*\psi(r) + \pi(r)v_p^*\right]dr \tag{14}$$

$$0 = \frac{\partial^2\psi(r)}{\partial r^2} + \frac{1}{r}\frac{\partial\psi(r)}{\partial r} + \omega^2\langle\rho_q^*(r)\rangle \tag{15}$$

where ¶ is a factor that guarantees the normalization of the distribution of the polymer conformations, $P(\alpha)$, and the dimensionless charge density obeys

$$\langle\rho_q^*(r)\rangle = \frac{\langle\rho_q(r)\rangle v_w}{e} = \frac{q_p^* f(r)\langle\phi_p(r)\rangle}{v_p^*} + \sum_{i\in\text{ions}}\frac{q_i^*\phi_i(r)}{v_i^*} \tag{16}$$

The superscript bulk at $\phi_i^{\text{bulk}} = \rho_i^{\text{bulk}}v_i$ in Eq. (11) refers to the bulk values of the parameters. One has $\rho_i^{\text{bulk}} = C_i^{\text{bulk}}N_A$ where $C_{\text{K}^+}^{\text{bulk}} = C_{\text{KCl}}$, $C_{\text{Cl}^-}^{\text{bulk}} = C_{\text{K}^+}^{\text{bulk}} + C_{\text{H}^+}^{\text{bulk}} - C_{\text{OH}^-}^{\text{bulk}}$ for pH ≤ 7 and $C_{\text{K}^+}^{\text{bulk}} = C_{\text{Cl}^-}^{\text{bulk}} - C_{\text{H}^+}^{\text{bulk}} + C_{\text{OH}^-}^{\text{bulk}}$, $C_{\text{Cl}^-}^{\text{bulk}} = C_{\text{KCl}}$ for pH ≥ 7 and $C_{\text{H}^+}^{\text{bulk}} = 10^{-\text{pH}}$ M, $C_{\text{OH}^-}^{\text{bulk}} = 10^{14-\text{pH}}$ M.[21]

The pertinent boundary conditions completing the equation for the potential obtained in Eq. (15) are

$$\left.\frac{d\psi}{dr}\right|_{r=0} = 0, \qquad \left.\frac{d\psi}{dr}\right|_{r=1} = \sigma_s^* = \frac{\beta e R_{\text{pore}}}{\varepsilon_f}\sigma_s \tag{17}$$

The system of coupled equations given by Eqs. (11) to (17) must be solved simultaneously. In fact, by finding the solution of these equations, the equilibrium distribution of the ions, $\phi_i(r)$ and water molecules, $\phi_w(r)$, the electrical potential field, $\psi(r)$, osmotic pressure distribution, $\pi(r)$, and the polyelectrolyte chains' morphological properties including their local monomer distribution, $\langle\phi_p(r)\rangle$, local degree of ionization, $f(r)$ and probability distribution, $P(\alpha)$, can be found at different environmental conditions, i.e varying pH, C_{KCl}, degree of polymerization N, surface grafting density σ and surface charge density σ_s. The obtained functions are subsequently used (next sections) to both solve the conservation law of momentum equations and evaluate other parameters of interest.

To solve the system of equations numerically, the radial coordinate of the nanopore is binned into $M = R_{\text{pore}}/\delta$ layers of identical thickness δ and the equations are discretized using the finite difference method. To solve this discretized system, a representative set of geometry-compatible and self-avoiding chain conformations is generated as the input of the theory. We use the `gensaw` code[66] to produce this representative sample of polymer chains. We assumed fully flexible chains and used the rotational isomeric state (RIS) model with constant bond length ℓ, constant bond angle 68°, and three equally possible states of trans, gauche$^+$, and gauche$^-$ with the same internal energy. We have written a new add-on code to `gensaw` for post-processing its output and extracting out the required information, including the number of monomers

residing in each of the M grid nodes. The code is general and can be used for 3D cases as well. Moreover, in this study, because the size of the mesh is chosen to be much smaller than the size of the monomers, we have added an option for the 1D case that can split the monomers and then find the portion of each monomer that resides in each grid node.

We recall that the molecular theory presented here is an equilibrium theory that predicts equilibrium polymer conformations. If the external perturbation arising from the pressure-driven flow is sufficiently small, the equilibrium structure will be similar to that in the steady state.[56] In a previous work, it was shown that using the equilibrium structure to determine steady-state properties in the case of voltage-driven ion fluxes is an excellent approximation for long nanochannels ($L_{\rm pore} \gtrsim 1$ μm).[65] Ignoring the perturbation imposed by the pressure gradient on the ionic distribution as well as on the polyelectrolyte layer is an extensively used approximation.[40,41,43–45] Thus, as a first-order approximation, in this work we will neglect the effect of the solvent and ion fluxes on the polymer conformations, ion density profiles and state of ionization, and we will determine the transport properties of the system from the equilibrium structure over a limited range of $\Delta P/L_{\rm pore}$ in Section III.

This approximation can be relaxed in the future at the cost of increasing the complexity of the theoretical framework.[56,67]

In order to evaluate $I_{\rm str}$ of the streaming current as well as the strengths $E_{\rm str}$ and $B(r)$ of the perpendicular electric and induced magnetic fields, i.e., $\mathbf{E}_{\rm str} = E_{\rm str}\mathbf{e}_Z$ and $\mathbf{B}(r) = \pm B(r)\mathbf{e}_\theta$, we need to find the velocity distribution. We start with the case of the ESC mode, followed by the OEC mode.

A. External short-circuited (ESC) mode

In this case, an ESC electrical connection is made between the reservoirs so that the reservoirs are maintained at the same potential. This can be approximated experimentally through placing a standard platinum electrode in each reservoir and connecting them by a wire. The evaluation of the velocity field requires to solve the mathematical representation of the momentum conservation law. The flow is assumed to be both steady and fully developed and there is no induced electrical field ($E_{\rm str} = 0$) because both reservoirs have the same electric potential in this case. The only volumetric force is therefore the drag created by the polyelectrolyte brushes. The widely accepted approach to account for the drag force is to consider a volumetric resistive force proportional to the velocity, which is equivalent to modeling the PEL as a porous medium utilizing the Brinkman equation. Such a resistive force is given as $F_{\rm PEL}U_z$, where $F_{\rm PEL}(r) = \mu(\langle\phi_p(r)\rangle/l_e)^2$ is the position-dependent hydrodynamic frictional coefficient of the PEL and l_e is the effective monomer size. As a consequence, the general momentum equation in the axial direction reduces to the following form[49,58,68,69]

$$\frac{\mu}{R}\frac{\partial}{\partial R}\left(R\frac{\partial U_z}{\partial R}\right) - hF_{\rm PEL}U_z - \frac{dP}{dZ} = 0 \qquad (18)$$

where quantities U_z, P and μ denote the Z-component of the velocity field, pressure field and dynamic viscosity, respectively. It should be pointed out that $F_{\rm PEL} = \mu/k(r)$ can be expressed in terms of the local permeability $k(r)$ of the brush layer, which is related to the monomer volume fraction $\langle\phi_p(r)\rangle$ via $k(r) = (l_e/\langle\phi_p(r)\rangle)^2$.[70,71] The auxiliary parameter h equals unity inside the grafted layer and zero within the electrolyte. We introduce the following characteristic velocity U_0, velocity field $u(r)$, and dimensionless hydrodynamic frictional coefficient ζ (characterizing a hypothetical PEL at $\langle\phi_p(r)\rangle = 1$) via

$$U_0 = \frac{R_{\rm pore}^2}{\mu}\frac{dP}{dZ}, \qquad u(r) = \frac{U_z(r)}{U_0}, \qquad \zeta = \frac{R_{\rm pore}}{l_e} \qquad (19)$$

to obtain the following equation (here and below, ϕ_p stands for $\langle\phi_p(r)\rangle$)

$$\frac{1}{r}\frac{\partial}{\partial r}\left(r\frac{\partial u}{\partial r}\right) - h\zeta^2\phi_p^2 u = 1 \qquad (20)$$

with the symmetry and Navier slip conditions[72]

$$\left.\frac{\partial u}{\partial r}\right|_{r=0} = 0, \qquad u(r=1) = -l_{\rm slip}\left.\frac{du}{dr}\right|_{r=1} \qquad (21)$$

where $l_{\rm slip}$ is a dimensionless slip coefficient. Note, that U_0 and u are negative, while U_z is positive. By solving Eqs. (18) to (21) using a finite difference method and the polymer volume fraction $\phi_p(r)$ obtained previously, we can calculate the velocity field $u(r)$. The streaming current is then given by

$$I_{\rm str} = \int_0^{R_{\rm pore}} \rho_e(R)U_z(R)2\pi R dR = I_{0,\rm str}i_{\rm str} \qquad (22)$$

where $\rho_e(R) = \sum_{i\in\{\rm ions\}}\rho_i = \sum_{i\in\{\rm ions\}}\phi_i q_i/\nu_i$ is the net charge density of the mobile ions at radius R, $I_{0,\rm str} = 2\pi R_{\rm pore}^2 eU_0/\nu_w$ is a numerical (negative and constant) prefactor, and the (positive) dimensionless streaming current given by

$$i_{\rm str} = \int_0^1 \sum_{i\in\{\rm ions\}} \frac{\phi_i(r)q_i^*}{\nu_i^*}u(r)rdr \qquad (23)$$

Substitution of the constant parameters mentioned in Table I results in $I_{0,\rm str} = 536\,\Delta P/L_{\rm pore}$, where $I_{0,\rm str}$, ΔP, and $L_{\rm pore}$ are taken here in units of nanoampere, bar and micrometer, respectively. To determine the magnetic fields, a closed circular loop of radius r is considered. According to Ampere's law, we have

$$\oint \mathbf{B}\cdot d\mathbf{l} = 2\pi\mu_p\int_0^R j(R)RdR \qquad (24)$$

where μ_p is the permeability, and $j(R)$ is the ionic flux density passing through the pore in the selected closed circular loop, which is equal to $\rho_e(R)u(R)$ for the ESC case. Moreover, due to symmetry considerations, the magnetic field has a constant magnitude around the loop, therefore, we have

$$B(r) = B_0 B^*(r) \qquad (25)$$

where $B_0 = \mu_p R_{\rm pore} eU_0/\nu_w$ absorbs the (negative) numerical prefactor, and the dimensionless magnetic field strength at r is given by

$$B^*(r) = \frac{\int_0^r \sum_{i\in\{\rm ions\}}\phi_i(r')q_i^*u(r')r'dr'/\nu_i^*}{r} \qquad (r \le 1) \quad (26)$$

The coefficients of the relative magnetic permeability of air and water, representative of the outside and inside environments, are 1.00000037 and 0.99999, respectively, and both are assumed equal 1 in this study. Upon replacing the values outlined in Table I, one obtains $B_0 = 5360\Delta P/L_{\text{pore}}$, where B_0, ΔP, and L_{pore} are in nanoTesla, bar and micrometer, respectively. Because we know the volume fraction profiles $\phi_i(r)$ and the velocity field $u(r)$, the integrals in Eqs. (23) and (26) can be calculated numerically using the 7 points composite Newton-Cotes formula.

Upon comparing Eq. (23) with Eq. (26) the outside magnetic field distribution can be expressed in terms of the amount $B^*(1)$ of the dimensionless magnetic field at $r = 1$ from Eq. (26), or alternatively in terms of i_{str} as

$$B^*(r) = \frac{B^*(1)}{r} = \frac{i_{\text{str}}}{r} \qquad (r \geq 1) \tag{27}$$

B. Open external circuit (OEC) mode

In this case, there is no external electrical connection between the two reservoirs and due to the accumulation (depletion) of the mobile counterions in the lower end (upper end) of the nanochannel, there is an imbalance of net charges in the vicinity of the entrance and exit of nanopore inducing a streaming potential. In this case the momentum conservation equation reads

$$\frac{\mu}{R}\frac{\partial}{\partial R}\left(R\frac{\partial U_z}{\partial R}\right) - hF_{\text{PEL}}U_z - \frac{dP}{dZ} + \rho_e E_{\text{str}} = 0 \tag{28}$$

By using the previously defined dimensionless parameters and adding the following one:

$$E^*_{\text{str}} = \frac{E_{\text{str}}}{E_0}, \qquad E_0 = \frac{v_w}{e}\frac{dP}{dZ} \tag{29}$$

then Eq. (28) becomes, using ρ_e defined after Eq. (22),

$$\frac{1}{r}\frac{\partial}{\partial r}\left(r\frac{\partial u}{\partial r}\right) - h\zeta^2\phi_p^2 u - 1 + \sum_{i\in\{\text{ions}\}}\frac{\phi_i(r)q_i^*}{\nu_i^*}E^*_{\text{str}} = 0 \tag{30}$$

where E^*_{str} is an unknown negative parameter, because $E_{\text{str}} > 0$ and $E_0 < 0$. Using in this equation the constant values reported in Table I, we obtain $E_0 = 18.75\Delta P/L_{\text{pore}}$, where E_0, ΔP, and L_{pore} are in volt per meter, bar and micrometer, respectively. The velocity field can be obtained from the superposition of the velocity u_P due to the applied pressure gradient and the velocity u_E created by the induced electrical field, that is $u = u_P + E^*_{\text{str}}u_E$ where dimensionless u_P and u_E are obtained from the following two equations

$$\frac{1}{r}\frac{\partial}{\partial r}\left(r\frac{\partial u_P}{\partial r}\right) - h\zeta^2\phi_p^2 u_P - 1 = 0 \tag{31}$$

$$\frac{1}{r}\frac{\partial}{\partial r}\left(r\frac{\partial u_E}{\partial r}\right) - h\zeta^2\phi_p^2 u_E + \sum_{i\in\{\text{ions}\}}\frac{\phi_i(r)q_i^*}{\nu_i^*} = 0 \tag{32}$$

The streaming current arises due to the convection mode of transport of the ions and can thus be evaluated using Eq. (22)

$$I_{\text{str}} = \int_0^{R_{\text{pore}}} \rho_e U_z(R) 2\pi R dR = I_{0,\text{str}}(i_{\text{str},P} + i_{\text{str},E}) \tag{33}$$

where $i_{\text{str},P}$ and $i_{\text{str},E}$ are the dimensionless streaming currents due to the imposed pressure gradient and the induced streaming potential, respectively,

$$i_{\text{str},P} = \int_0^1 \sum_{i\in\{\text{ions}\}}\frac{\phi_i(r)q_i^*}{\nu_i^*}u_P(r)rdr \quad \equiv X_P, \tag{34}$$

$$i_{\text{str},E} = E^*_{\text{str}}\int_0^1 \sum_{i\in\{\text{ions}\}}\frac{\phi_i(r)q_i^*}{\nu_i^*}u_E(r)rdr \quad \equiv X_E E^*_{\text{str}} \tag{35}$$

However, because of the induced streaming potential, there is also a migration flux of the ions, which results in a conduction current inside the pore. This conduction current, written as $I_{\text{con}} = I_{0,\text{str}}i_{\text{con}}$, can be expressed as

$$i_{\text{con}} = \frac{2\pi E_{\text{str}}}{I_{0,\text{str}}}\int_0^{R_{\text{pore}}} \sum_{i\in\{\text{ions}\}}\lambda_i C_i R dR \quad \equiv X_{\text{con}}E^*_{\text{str}} \tag{36}$$

where λ_i is the molar electric conductivity of species i and

$$X_{\text{con}} = \frac{E_0}{eU_0N_A}\int_0^1 \sum_{i\in\{\text{ions}\}}\frac{\lambda_i\phi_i(r)}{\nu_i^*}rdr \tag{37}$$

In the steady states, the net ionic current passing through the pore should vanish, that is $I_{\text{con}} + I_{\text{str}} = 0$. This provides an equation to find the unknown variable E^*_{str} as the following

$$E^*_{\text{str}} = -\frac{X_P}{X_E + X_{\text{con}}} \tag{38}$$

where we recall that the X's are all positive, E^*_{str} is negative. By finding E^*_{str}, one can find the velocity field from $u = u_P + E^*_{\text{str}}u_E$ and the streaming current from Eqs. (33)–(35). Finally, through using the Ampere's law, the magnetic field strength inside the pore is obtained as

$$B(R) = \frac{\mu_p\int_0^R j(R')R'dR'}{R} = \frac{\mu_p R_{\text{pore}}\int_0^r j(r')r'dr'}{r} \tag{39}$$

where $j(r)$ is the strength of the total ionic flux density $\mathbf{j}_{\text{str}}(r) + \mathbf{j}_{\text{con}}(r)$ of the ions due to the convection and conduction modes of transport given as

$$j(r) = \frac{eU_0}{\nu_w}\sum_{i\in\{\text{ions}\}}\frac{\phi_i(r)q_i^*}{\nu_i^*}u(r) + \frac{E_0E^*_{\text{str}}}{N_A\nu_w}\sum_{i\in\{\text{ions}\}}\frac{\lambda_i\phi_i(r)}{\nu_i^*} \tag{40}$$

Inserting (40) into (39), and using dimensionless r and B^*, the final expression for the strength $B^*(r) = B^*_{\text{str}}(r) + B^*_{\text{con}}(r)$ of the dimensionless magnetic field is

$$B^*(r) = \frac{1}{r}\int_0^r \sum_{i\in\{\text{ions}\}}\left[q_i^*u(r') + \frac{E_0E^*_{\text{str}}}{eU_0N_A}\lambda_i\right]\frac{\phi_i(r')}{\nu_i^*}r'dr' \tag{41}$$

where E^*_{str} is provided by Eq. (38) with Eqs. (34), (35), and (37).

C. Other macroscopic quantities

Streaming current generation has been identified to be a mechanism of electrochemomechanical energy conversion,

i.e., conversion of mechanical energy (in the form of pressure-driven transport) and chemical energy (in the form of EDL ions) to electrical energy associated with the generation of the streaming potential. Having obtained the velocity field and streaming potential, this quantity can be quantified by the ratio between output and input energy,

$$\varepsilon = \frac{P_{\text{out}}}{P_{\text{in}}} \tag{42}$$

where the two positive energies are determined by

$$P_{\text{out}} = -\frac{I_{\text{str}} E_{\text{str}}}{4}, \qquad P_{\text{in}} = -\frac{dP}{dZ} Q_{\text{in}} \tag{43}$$

and where Q_{in} is the input volume flow rate for the purely pressure-driven flow without considering the effect of induced back electroosmotic transport. Using our dimensionless parameters, Eq. (42) with Eq. (43) can be cast into the following form,

$$\varepsilon = \frac{i_{\text{str}} E^*_{\text{str}}}{4Q^*_{\text{in}}} = \frac{(i_{\text{str},P} + i_{\text{str},E}) E^*_{\text{str}}}{4Q^*_{\text{in}}} = -\frac{X_{\text{con}} X_P^2}{4Q^*_{\text{in}} (X_{\text{con}} + X_E)^2} \tag{44}$$

where $Q^*_{\text{in}} = \int_0^1 u(r) r dr$, and where we have used Eqs. (34), (35), and (38) to rewrite the expression.

The streaming conductance is determined as

$$G_{\text{str}} = \frac{I_{\text{str}}}{\Delta P} \tag{45}$$

wherein $\Delta P = P_{\text{up}} - P_{\text{down}} < 0$ is the pressure difference between the two reservoirs. Through defining positive $G_0 = 10^{12} I_{0,\text{str}} / \Delta P = 5.36 / L_{\text{pore}}$, where G_0, and L_{pore} are in picoampere per bar, and micrometer, respectively, the dimensionless streaming conductance is calculated as $G^*_{\text{str}} = G_{\text{str}} / G_0$.

It is well-known that the induced streaming potential invariably triggers an electroosmotic transport in a direction opposing the purely pressure-driven fluid motion. As a consequence, the net flow rate is smaller than that of the pure pressure-driven flow rate. This decrease of the net flow rate, known as the electroviscous effect, is usually expressed in terms of an effective viscosity ratio defined as

$$\frac{\eta_{\text{eff}}}{\eta} = \frac{\int_0^1 u_P(r) r dr}{\int_0^1 u(r) r dr} \tag{46}$$

where u_P is the dimensionless pure pressure-driven flow field. Moreover, the mean degree of ionization of polyelectrolyte chains and the mean value of magnetic field inside the pore can be respectively obtained as

$$\langle f \rangle = \frac{\int_0^1 f(r) \langle \phi_p(r) \rangle r dr}{\int_0^1 \langle \phi_p(r) \rangle r dr} \tag{47}$$

$$\langle B^* \rangle = 2 \int_0^1 B^*(r) r dr \tag{48}$$

and similarly for the contributions $\langle B^*_{\text{str}} \rangle$ and $\langle B^*_{\text{con}} \rangle$ to the magnetic field. Most of the quantities summarized in this section can only be evaluated for the OEC case, including Eqs. (42)–(44), and (46) since there is no streaming potential for the ESC mode, while Eqs. (45), (47), (48) apply to both cases.

This study is mostly focused on the numerical solution and the results are mainly reported by solving the equations brought in the current section. To validate the numerical results and to provide some explicit solutions under special circumstances, analytical solutions are presented in the appendix A. These solutions require several simplifying assumptions, such as low surface potential, a fixed thickness of the the soft layer, fixed charge density and the absence of any morphological properties of the polymer chains. Numerical solutions addressing these approximations are presented in this study; the analytical solutions are used to validate them. The derived analytical solutions brought in the appendix A are expressed in terms of the assumed constant soft layer thickness, hydrodynamic frictional coefficient and polyelectrolyte charge density. Although these assumptions are extensively used in previous studies, they are generally not accurate, but still hold true at some situations like low-potential surfaces and either high or low pHs, where all the the chargeable sites along the polyelectrolyte brushes are completely neutral or charged, respectively. As a consequence, these formulas can be treated independently provided that the PEL friction coefficient, polymer brush height, and charge density of the polymer brushes are given as inputs to these relations and they will provide answers in accord with these approximations. For sure, to obtain accurate results and to include the pH-responsiveness nature of the PE-chains, the equations derived in the molecular theory section should be solved.

Under certain conditions, the parameters required for the simple analyical theory can be evaluated by averaging the numerical results obtained in section II. These parameters are:

$$\delta_s = \sum_{\alpha} P(\alpha) \delta(\alpha) \tag{49}$$

$$\langle \rho_{\text{PEL}} \rangle = \frac{2}{v_w} \frac{\int_0^1 \langle \phi_p(r) \rangle f(r) q^*_p r dr}{1 - r_b^2} \tag{50}$$

$$\langle \langle \phi_p \rangle \rangle = \frac{2 \int_0^1 \langle \phi_p(r) \rangle r dr}{1 - r_b^2} \tag{51}$$

where $\delta(\alpha)$ is the thickness of polyelectrolyte chain at conformation α, and $\langle \rho_{\text{PEL}} \rangle$ and $\langle \langle \phi_p \rangle \rangle$ are the mean number density of polyelectrolyte charges and mean polymer volume fraction obtained by averaging in the radial direction, respectively. To make the best possible comparison between the analytical and numerical results, we obtain the value of the constant friction coefficient F_* in (A28) from the earlier definition of $F_{\text{PEL}}(r)$, $F_{\text{PEL}}(r) = \mu(\langle \phi_p(r) \rangle / l_e)^2$, and replacing the r-dependent $\langle \phi_p(r) \rangle$ by $\langle \langle \phi_p \rangle \rangle$. For the same goal, the average parameters, δ_s and $\langle \rho_{\text{PEL}} \rangle$ are now respectively used as the fixed soft layer thickness and polyelectrolyte number density in equation (A22).

III. Results and discussion

In this section, the interwoven effects of solution pH, background salt concentration C_{KCl}, polyelectrolyte grafting density σ, surface charge density σ_s, friction ζ, slip coefficient l_{slip} and degree of polymerization N on the streaming poten-

Parameter	Units	Value
T	[K]	298.15
μ	[Pa.s]	0.001
pK_a	—	5.2
R_{pore}	[nm]	20
l	[nm]	0.5
l_e	[nm]	0.5
ε_f	[F.m^{-1}]	$78.5 \times 8.854 \times 10^{-12}$
N	—	10
μ_p	[H.m^{-1}]	$4\pi \times 10^{-7}$
e	[C]	1.602×10^{-19}
k_{B}	[m^2.kg.s^{-2}.K^{-1}]	1.3806×10^{-23}
N_A	[mol^{-1}]	6.022×10^{23}

TABLE I. Fixed values of physiochemical parameters used in the modeling, temperature T, dynamic viscosity μ, pore radius R_{pore}, bond length l, effective monomer size l_e, solution permittivity ε_f, polymerization degree N, and magnetic permeability μ_p, along with values of physical constants.

Parameter	K^+	H^+	Cl^-	OH^-	p	w
$\nu_i \times 10^{30}$ [m^3]	82	30	82	30	95	30
$\lambda_i \times 10^3 \left[\frac{\mathrm{S.m^2}}{\mathrm{mol}}\right]$	7.352	34.98	7.634	19.76	—	—
q_i [e]	+1	+1	-1	-1	+1	—

TABLE II. Fixed values of species-specific physiochemical parameters used in the modeling: volume ν_i, molar electric conductivity λ_i, and electric charge q_i of species i.

tial (SP) E_{str}, streaming conductance G_{str}, electroviscous effect η_{eff}/η, electrochemomechanical energy conversion efficiency ε, mean degree of ionization $\langle f \rangle$ and magnetic field distribution $B(r)$ and its mean $\langle B \rangle$ are investigated. All the results are obtained using the physicochemical parameters summarized in Tables I and II unless otherwise stated.

Results to be presented are valid for arbitrary pressure gradients and pore lengths, as long as the assumptions underlying the theory are met. The results are presented in terms of reduced units. The equilibrium approximation fails if the configuration of the brushes gets considerably affected by the pressure gradient forces, i.e., if the shear rate exceeds a certain threshold. The maximum of the internal shear rate is realized for a solid-state nanopore when externally short circuited. This stems from the lack of opposing forces created by the either induced electrical field or PE frictional forces against the pressure gradient. We find an average shear rate $\dot{\gamma}_{\mathrm{ave}}$ in accord with this situation by averaging the first derivative of Eq. (A8) with respect to the r-direction, resulting in $\dot{\gamma}_{\mathrm{ave}} \approx U_0/3R_{\mathrm{pore}}$. As long as the approximations are met, this shear rate provides an upper limit for shear rates in soft nanopores, as the shear rate tends to decrease with the amount of tethered polymer. The polymer can be considered to be close to equilibrium, if $\tau\dot{\gamma} < 1$ where τ is the longest relaxation time of the polymer chain, which in turn depends on the molecular weight and polymer density, in particular. Results therefore apply if one chooses to operate at $\Delta P/L_{\mathrm{pore}} < 3\mu/(R_{\mathrm{pore}}\tau)$ for a ESC soft nanopore with negligible PE grafting density, and correspondingly larger thresholds for soft nanopores with either higher surface grafting density or the OSC case. Upon inserting a typical value of 1 µs for the relaxation time of a polymer chain, and using values from Table I, this gives $\Delta P/L_{\mathrm{pore}} < 1.5$ bar/µm.

FIG. 2. A comparison between the results of the molecular theory modeling and those obtained from analytical solutions (Appendix A) using a set of parameters for which the assumptions of the analytical theory are met. (**a**,**c**) Potential $\psi(r)$ (using Eq. (A5) in panel (a) in Eqs. (A25) and (A26) in panel (c)) and velocity $u(r) = U_z(r)/U_0$ distributions (using Eq. (A8) in panel (a) and Eqs. (A32) and (A33) in panel (c)) and (**b**,**d**) magnetic field $B^*(r) = B(r)/B_0$ for both OEC and ESC cases versus reduced radial location $r = R/R_{\mathrm{pore}}$ (using Eqs. (A12) and (A13) for ESC case and Eq. (A19) for OSC case in panel (b), and Eqs. (A38), (A39), and (A40) for ESC case and Eqs. (A51) and (A52) for OSC case in panel (d)). Note that in (b, d), the left and bottom axis are used for the ESC case, and the right and top axis are used for the OEC case. Calculation conditions: (a,b) $\sigma = 0.0$ chains/nm^2 (no PEL, solid-state nanopore with surface charges only), $C_{\mathrm{KCl}} = 0.1$ M, (c,d) $\sigma = 0.05$ chains/nm^2 (PEL grafted nanopore), $C_{\mathrm{KCl}} = 0.01$ M. Other calculation parameters for all panels: solution pH = 8 (PEL is nearly neutral), slip coefficient $l_{\mathrm{slip}} = 0$, and surface charge density $\sigma_s = 0.01e.\mathrm{nm}^{-2}$.

To make a further example about the conversion to real units, before presenting results in dimensionless form, consider a modest applied pressure[16] ($\Delta P = 1$ bar) in a nanopore with longitudinal length $L_{\mathrm{pore}} = 1$ µm. For this example, the conversion factors become $E_0 = 18.75$ V/m, $I_0 = 536$ nA, $B_0 = 5360$ nT, and $G_0 = 5.36$ pA/bar. Such values fall within the range of experimentally accessible magnitudes for nanoporous systems.

The presentation of the results starts with a comparison between the predictions of the molecular theory and PB-DB (Poisson-Boltzmann with Debye-Hückel) approximation, see Fig. 2. The parameters were selected to satisfy the condition of low surface potential (required for Debye-Hückel approximation) as it is evidenced in panels (a) and (c). These panels show an excellent agreement between the two models. A comparison of panels (a) and (c) reveals that increasing C_{KCl} results in a faster decay of the electrostatic potential because the Debye length gets shorter. It is further visible from panels (b) and (d) that for the ESC case, the strength of the magnetic field increases with increasing distance to the central axis and reaches its maximum near the solid interface. This result is rooted in the fact that the induced magnetic field at radial location R arises from the integral of the flux of the ions passing through a closed circular loop with the radius of that location. In the ESC mode, there is no streaming potential inside the pore because the reservoirs have the same voltage, and thus the only contributing term to the ionic flux is convection from purely pressure-driven flow. That flux integral is maximum close to the wall, leading to a maximum of B^* in that region. Moreover, for the case of $C_{\mathrm{KCl}} = 0.1$ M (panel b) counterions are gathered in a thin layer close to the nanopore surface because of the small Debye length, and the net mobile ion concentration and, accordingly, the ionic fluxes almost vanish in the central region of the pore, which leads to a very small B^* in this area.

FIG. 3. Variation of mean degree of ionization $\langle f \rangle$ versus (a) pH at $\sigma_s = 0.05\ e.\text{nm}^{-2}$ with $\sigma = 0.1$ chains/nm^2 (black lines) or $\sigma = 0.6$ chains/nm^2 (blue lines), (b) C_{KCl} at $\sigma = 0.1$ chains/nm^2 with $\sigma_s = 0.05\ e.\text{nm}^{-2}$ (black lines) or $\sigma_s = 1\ e.\text{nm}^{-2}$ (blue lines).

However, for the OEC case the situation is different. In this case, due to the induced streaming potential inside the pore, the conduction term as well as the advection term from back electroosmosys play important roles in determining the value of B^*. For $C_{\text{KCl}} = 0.1$ M (panel b), these terms are dominant making the value of B^* negative, which means that the magnetic field is in the negative direction of θ-axis all over the pore while for $C_{\text{KCl}} = 0.01$ M (panel d) the convection transport overcomes near the interface and makes the value of B^* positive in this regime. Note that there is no net flux of ions in the OEC case, therefore, $B^* = 0$ at the wall of the channel and outside it.

We mention here that all the results reported in the upcoming Figs. 3-12 are obtained by the full numerical calculation of the molecular theory approach elaborated in section II. Moreover, the values $N = 10$ and $R_{\text{pore}} = 20$ nm are considered in all the results, unless otherwise stated. The influence of pH and bulk salt concentration on the mean degree of ionization, $\langle f \rangle$, is presented in Fig. 3. A decrease in the solution pH leads to an increase in $\langle f \rangle$. The reason of this behavior is that by decreasing pH, the concentration of hydroxyl ions decreases, which shifts the equilibrium reaction, Eq. (1), toward the charged species to compensate the lack of hydroxyl ions in the solution according to the Le Chatelier principle. It is also visible that by increasing the surface grafting density of polyelectrolyte chains, $\langle f \rangle$ is decreased. This effect is a consequence of charge regulation.[63,73] The electrostatic repulsions between the charged segments within the brush layer increases the free-energy cost of creating a new charged segment by protonation of a neutral one, thus the $\langle f \rangle$ of the segments in the brush is smaller than that expected for the same chemical species free in solution. This effect explains why $\langle f \rangle < 0.5$ for pH = pKa, in 3. Increasing the surface coverage of the PEL augments the electrostatic repulsions in the system and, therefore, decreases the average degree of protonation,$\langle f \rangle$.

In Fig. 3(b) the effect of C_{KCl} on $\langle f \rangle$ is illustrated. As can be seen, increasing the bulk salt concentration increases $\langle f \rangle$. This effect results from the fact that added salt screens the electrostatic interactions between the polyelectrolyte segments, therefore decreasing the magnitude the charge-regulation effect. As a consequence, $\langle f \rangle$ increases as it approaches the value expected for the free species in solution.[74] Moreover, panel (b) shows that increasing the surface charge density, decreases $\langle f \rangle$, which can be also attributed to the electrostatic repulsions between the surface charges and the charged polyelectrolyte segments, in accordance to the charge-regulation mechanism described above. It is also worthwhile to observe that $\langle f \rangle \approx 0$ ($\langle f \rangle \approx 1$) for pH = 8 (pH = 1), as expected from the concentration of protons in solution.

The effect of pH on the electrical field, streaming conductance, effective viscosity ratio and efficiency for the OEC system is shown in Fig. 4. With increasing pH, the amplitude of induced electrical field $E_{\text{str}} = E^*_{\text{str}} E_0$ (Eq. (29)) is first increased and then decreased (panel a). The increasing trend of E_{str} for acidic pH values can be attributed to the fact that when pH gets increased to values close to the neutral solution, the concentration of protons is considerably diminished. Therefore, the thickness of the electric double layer increases, which enhances the advection of the charge density gradient, and consequently enhances the SP. As expected, this effect is more obvious for low values of background salt concentration ($C_{\text{KCl}} = 0.001$ M and 0.01 M) than for large salt concentrations. For high pH values the reverse trend of SP is rooted in two main factors; first there is the decrement of $\langle f \rangle$ that leads to a depletion of mobile ionic charges within the PEL, ρ_e, and consequently lower the advection of the charged species inside the pore. The second factor is the increment of the concentration of OH^- ions, which reduces the Debye length and increases the conductivity, X_{con}, because of the high value of λ_{OH^-}, thus lowering E_{str}.

FIG. 4. (a) dimensionless streaming electrical field $E^*_{\text{str}} = E_{\text{str}}/E_0$, (b) dimensionless streaming conductance $G^*_{\text{str}} = G_{\text{str}}/G_0$, (c) effective viscosity ratio η_{eff}/η, and (d) efficiency ε (%) versus pH of the solution for different values of C_{KCl}. The remaining parameters are $\sigma = 0.1$ chains/nm^2, $\sigma_s = 0.05\ e.\text{nm}^{-2}$ and $l_{\text{slip}} = 0$.

As shown in Fig. 4(b) there is a decreasing trend for the reduced streaming conductance $G^*_{\text{str}} = G_{\text{str}}/G_0$ (Eq. (45)) with increasing pH. The streaming conductance inside the pore is affected by the advection of the ions due to both purely pressure-driven flow and back eletroosmotic transport. The advection from back electroosmotic transport happens because of the induced SP, which is always in the opposite direction of that from purely pressure-driven flow. For increasing pH, $\langle f \rangle$ decreases, and the concentration of net mobile ionic charges reduces. Thus, as the pH increases from highly acidic to closely neutral values, the streaming potential is enhanced (see panel a), which strengthens the opposite convection transport. These two effects result in the decreasing trend of G_{str}. We see furthermore that for high pH values, as C_{KCl} increases, the streaming conductance decreases. This effect is due to the reason that at high pH values, the concentration of net mobile ionic charges near the wall is low. Increasing C_{KCl} reduces the Debye-length, so charges get confined to an area close to the walls, where velocity is small, thereby causing the advection of the ions to vanish.

The plot of effective viscosity ratio, defined in Eq. (46), versus pH is shown in Fig. 4(c). Generally speaking, increasing the pH has three consequences: (1) because of the reduction of $\langle f \rangle$, the net mobile charge density decreases, decreasing volumetric body forces and, consequently, the back electroosmotic velocity, (2) E_{str} is amplified for low to medium pH ranges, as shown in panel (a), and (3) the concentration of the ions considerably decreases with increasing pHs, thus increasing the thickness of the EDL, which is then not limited to the area close to the wall (where the resistive frictional force is max-

FIG. 5. (a) Dimensionless streaming electrical field, (b) dimensionless streaming conductance, (c) effective viscosity ratio, and (d) efficiency (%) versus C_{KCl} of the solution for different values of pH. The remaining parameters are $\sigma = 0.1$ chains/nm^2, $\sigma_s = 0.05$ e.nm^{-2} and $l_{\mathrm{slip}} = 0$.

imum). The latter two effects (occuring for low to moderate pH) decreases the overall fluid motion, u, which results in an ascending variation of η_{eff}/η with pH. On the other hand, for pH $> \sim 4$, the first factor plays the most important role, which results in a high total velocity magnitude and consequently a reverse trend for η_{eff}/η.

The variation of the energy-conversion efficiency ε (42) with pH results from the variations of E_{str} and G^*_{str} with pH shown in panels Fig. 4(a) and (b), respectively. Since the input energy is fixed and does not change for different values of pH and C_{KCl}, the variation of ε is only determined by the multiplication of these two quantities, resulting in the plot shown in panel (c). As can be seen, by controlling the pH and background salt concentration, we can reach efficiencies higher than 4%, which is a relatively high value. Actually, this condition happens by adjusting pH to medium values (pH $\approx$ 4) and using low bulk salt concentrations, $C_{\mathrm{KCl}} = 0.001$ M (which produce a large overlap of the EDL).

The effect of C_{KCl} on the streaming potential is shown in Fig. 5(a). Two important consequences arise from increasing the bulk salt concentration: (1) the thickness of the EDL decreases and this layer is confined to a region near the solid interface, where the velocity is small and (2) there is an enhacement of the degree of ionization of the PEL (as pointed out in Fig. 3(b)), as well as of the concentration of the net mobile ionic charges. While the first effect leads to a suppression of the advection of the charged species and the streaming potential, the second effect amplifies these variables. The interplay between these two effects determines the trend of E^*_{str} with C_{KCl}. As seen in panel (a), the first effect is dominant, resulting in a SP that monotonically decreases with the bulk salt concentration.

Figure 5(b) shows that G^*_{str} increases with C_{KCl} at pH = 1–5, while the trend is reversed at pH = 8. As C_{KCl} increases, E_{str} is diminished (as shown in panel a), resulting in lower back electroosmotic velocity; however, at the same time, it leads to the enhancement of ρ_e due to the increase of $\langle f \rangle$. These two effects cause the amplification of the streaming current for acidic pH values (pH = 1,3,5). However, for pH = 8 the concentration of net mobile ionic charges (i.e., the concentration of the counterions minus the concentration of the coions) is very low because the degree of ionization almost vanishes (see Fig. 3b). Under these conditions, increasing C_{KCl} confines this small concentration of net charges to the area close to the wall where velocity is insignificant, causing G^*_{str} to decrease.

The variation of the effective viscosity ratio η_{eff}/η with C_{KCl} is shown in Fig. 5(c). Increasing C_{KCl} leads to a higher degree of ionization, lowering the streaming potential and limiting the electric body forces to the soft layer region where the

FIG. 6. (a) Dimensionless streaming electrical field, (b) dimensionless streaming conductance, (c) effective viscosity ratio, and (d) efficiency (%) versus dimensionless PEL hydrodynamic frictional coefficient ζ for different values of pH, σ (in chains/nm^2), and C_{KCl} (in d). Lines with symbol corresponds to $C_{\mathrm{KCl}} = 0.1$ M and without symbols to $C_{\mathrm{KCl}} = 0.01$ M. The remaining parameters are $\sigma_s = 0.05$ e.nm^{-2} and $l_{\mathrm{slip}} = 0$.

resistive force is highest. The balance between these effects determines the resulting trend. For pH = 3 and 5, where $\langle f \rangle$ strongly increases with increasing C_{KCl}, c.f., Fig. 4(b), the former effect is dominant at low C_{KCl} , resulting in an initial increase of η_{eff}/η. However, at pH = 1 and pH = 8, the other two effects are influential, causing an enhancement of the overall velocity and consequently, a decrease of the viscosity ratio for all C_{KCl} values.

As explained before, the trend of ε is determined by the variation of the two quantities E_{str} and G_{str} plotted in Fig. 5(a) and (b). It is noteworthy that at pH = 1, although $\langle f \rangle$ has its maximum value, ε is even smaller than that at pH = 8 where $\langle f \rangle$ is almost zero. This result can be attributed to the high value of E_{str} at pH 8 that results from a thick electric double layer and a low $\langle f \rangle$ at that pH. Once again, the highest efficiency occurs here at moderate pHs values (pH = 5) and the lowest C_{KCl} studied (where EDL overlap is highest).

The effect of dimensionless PEL hydrodynamic frictional coefficient ζ defined in Eq. (19) is shown in Fig. 6. Increasing ζ, increases the resistive frictional force, which leads to a lower advection-driven accumulation of the charge density gradient, and so lowers E_{str} (panel a). In fact, increasing the hydrodynamic frictional coefficient causes two effects: (1) lowers E_{str} and, accordingly, the electrosmotic velocity in the opposite direction to the pressure-driven flow, and (2) hinders the motion of the fluid and ionic advection due to higher resistive forces. While the former effect enhances the streaming conductance, the latter one decreases it, so the interplay between these two effects determines the overall trend of G_{str}. In Fig. 6(b), the latter is dominant leading to a descending functionality of G_{str} with ζ. Moreover, by paying attention to the definition of the effective viscosity ratio, Eq. (46) , one can infer that the two mentioned factors affect η_{eff}/η in the same way. The first one increases the denominator of the ratio (46) by decreasing the induced electroosmotic velocity, and the second effect reduces the numerator because it reduces the fluid motion. Both effects cause η_{eff}/η to decrease with ζ, Fig. 6(c). In panel (d) of the same figure, we can see that the efficiency non-monotonically varies with ζ. For example for pH = 1 and $\sigma = 0.6$ chains/nm^2 there is an ascending-descending variation with ζ, while for the other cases a descending functionality is observed. This is rooted in the fact that increasing ζ decreases both the streaming potential and the streaming conductance (panels a and b), which causes the output energy P_{out} to decline as well, in line with Eq. (43). The same is true for the input energy P_{in} due to the increment of the resistive frictional force, so, the interplay between P_{in} and P_{out} leads to the various overall trends seen in Fig. 6(d).

Increasing surface coverage of the polyelectrolye, σ, en-

FIG. 7. Plots of (a) dimensionless streaming electrical field, (b) dimensionless streaming conductance, (c) effective viscosity ratio, and (d) efficiency (%) versus pH at different values of C_{KCl}, σ (in chains/nm^2), and l_{slip}. Lines with symbol correspond to $l_{\mathrm{slip}} = 0.1$ and without symbols to $l_{\mathrm{slip}} = 0$. The value of σ_s was fixed to 0.05 e.nm^{-2}.

FIG. 8. Plots of (**a**) dimensionless streaming electrical field, (**b**) dimensionless streaming conductance, (**c**) effective viscosity ratio, and (**d**) energy-conversion efficiency (%) versus pH at different values of C_{KCl}, σ, and degree of polymerization N. Lines with symbol belong to $\sigma = 0.6$ chains/nm^2 and without symbols to $\sigma = 0.1$ chains/nm^2. The value of σ_s is equal to 0.05 e.nm^{-2}.

hances both the resistive forces and the density of PEL electric charges. The former suppresses the fluid motion by increasing the resistive mechanical force. The latter effect, increased density of PEL charges, causes two effects: it increases the resistive electrical force due to the term ($\rho_e E^*_{\mathrm{str}}$) and it increases the advection-driven accumulation of the charge density gradient. The interplay between them determines how the ultimate fluid velocity varies with the surface grafting density. When ζ is high and the degree of ionization is small (which corresponds to pH = 8), the first effect (increase of resistive forces) becomes dominant, which leads to the decrease of the advection of charge density and fluid motion due to high mechanical resistive forces and consequently E_{str}, G_{str}, η_{eff}/η, and ε are lower for $\sigma = 0.6$ chains/nm^2 than for $\sigma = 0.1$ chains/nm^2. However, at pH = 1, where $\langle f \rangle$ is large, the opposite trend is observed for the energy-conversion efficiency. It is noteworthy to recall that the efficiency is a parameter that depends on the combination of all the independent parameters, for example Fig. 6(d) shows that for pH = 1 and $\sigma = 0.1$ chains/nm^2, ε is higher at $C_{\mathrm{KCl}} = 0.01$ M than at $C_{\mathrm{KCl}} = 0.1$ M, while the reverse is true for pH = 1 and $\sigma = 0.6$ chains/nm^2.

The effect of l_{slip} is inspected in Fig. 7. As shown, E_{str} increases with increasing l_{slip}. Generally, increasing the slip coefficient leads to a decrease of the frictional force at the solid interface, which enhances the fluid velocity and augments the advection of charged species and the accumulation of counterions in the lower end of the nanopore. Therefore, the streaming potential increases. At $C_{\mathrm{KCl}} = 0.1$ M the advection is weaker and the streaming potential is lower than at $C_{\mathrm{KCl}} = 0.1$ M because at $C_{\mathrm{KCl}} = 0.1$ M the EDL is thinner and more limited to the region close to the wall than at $C_{\mathrm{KCl}} = 0.001$ M. Fig. 7(b) shows that increasing l_{slip} has two major opposite effects: firstly, it enhances u_P leading to an increment of $i_{\mathrm{str},P}$, and consequently of i_{str}. Secondly, it increases E_{str}, so $i_{\mathrm{str},E}$ is magnified, which decreases i_{str}. Therefore, the interplay between these two opposite effects determines the ultimate trend of G_{str} at different conditions. In Fig. 7(c) it is visible that by increasing l_{slip}, the viscosity ratio is enhanced due to the amplification of the pressure-driven flow and the back electroosmotic velocity. Moreover it is seen that at pH > 6 and $C_{\mathrm{KCl}} = 0.1$ M, η_{eff}/η becomes almost unity, which is due to the insignificant back electroosmotic transport because of the very thin Debye length, and a negligible $\langle f \rangle$. The efficiency ε in Fig. 7(d) depends on the variation of E_{str} and i_{str}, as well as P_{in}. The behavior of E_{str} is shown in panel (a) and the variation of i_{str} is exactly the same as that of G_{str}, shown in panel (b). Noteworthily, increasing l_{slip} enhances P_{in} because of the decrease of the resistive force at the solid wall. Therefore, the interplay between all these parameters determine the trend of ε. Interestingly, increasing the slip coefficient in some conditions leads to a decrease in the efficiency of energy conversion. Moreover, it is noteworthy that increasing the polyelectrolyte grafting density can also lead to a decrease in efficiency in some conditions. The highest efficiency occurs for $\sigma = 0.1$ chains/nm^2, pH $\approx$ 4–5 and low salt concentration (C_{KCl} = 0.001 M).

The effect of the degree of polymerization is analyzed in Fig. 8. Increasing N both increases ρ_e and extends the resistive mechanical forces to central areas. For σ = 0.1 chains.nm^{-2} and $C_{\mathrm{KCl}} = 0.1$ M, the EDL is confined to a region close to the wall, thus the increase of ρ_e is more important than the enhancement of the mechanical forces. Therefore, under these conditions, the advection of the ions and, consequently, E_{str} are higher for $N = 20$ than for $N = 5$. However, at $C_{\mathrm{KCl}} = 0.001$ M, since the EDL is thick and expands into the central regions, frictional forces also become significant, leading to a decrease of the advection of the ions. Therefore, E_{str} for $N = 20$ is smaller than for $N = 5$. Furthermore, this trend also depends on σ because increasing σ affects both the frictional forces and the charge density of the brush. In this way, at low pHs and σ = 0.6 chains.nm^{-2}, E_{str} is higher for $N = 20$ than for $N = 5$. Fig. 8(c) shows that enhancing N increases the effective viscosity ratio, which is equivalent to the decrement of overall velocity (see Eq. (46)) and it is explained by the increase of the electrical body forces and, subsequently, the back electroosmotic velocity. Moreover, at basic pHs there is no significant difference between ρ_e for $N = 5$ and $N = 20$ and, thus, the electrical body forces are similar too, which causes η_{eff}/η to be almost the same for both $N = 5$ and $N = 20$. The value of the dimensionless streaming conductance depends on both ρ_e and the velocity. Increasing N leads to the decrement of the velocity (panel c) and, simultaneously, increases ρ_e. The balance between these effects determines the final trend of G_{str}. As can be seen, G_{str} is higher for $N = 20$ than for $N = 20$ for $\sigma = 0.1$ chains.nm^{-2} and acidic pHs, while for $\sigma = 0.6$ and $C_{\mathrm{KCl}} = 0.1$ M, the opposite trend is observed. Furthermore, at pH > 6, there is no significant difference between velocities (see panel c) and the net charge densities ($\langle f \rangle \approx 0$), hence, G_{str} is almost the same for $N = 5$ and $N = 20$. The variation of ε is shown in Fig. 8(d), which shows a maximum (relatively high) efficiency of $\approx$ 5%.

The effects of pH and C_{KCl} on the distribution of internal and external magnetic fields are shown in Fig. 9. As mentioned earlier, the induced magnetic field at location r is determined by the integral of the flux of the ions passing through a circle with the radius at that location. Panels a and b correspond to the ESC case. Panel a shows that by increasing C_{KCl}, the value of B^* near the solid interface ($r \approx 1$, corresponds to the maximum B^*) is increased, while the reverse trend is true

FIG. 9. Variation of $B^*(r)$ as a function of radial coordinate r for (**a**,**c**) different values of C_{KCl} at pH = 5 and (**b**,**d**) different values of pH at $C_{\mathrm{KCl}} = 0.01$ M. Panels (a,b) belong to the ESC case and (c,d) belong to the OEC case. The remaining parameters are $l_{\mathrm{slip}} = 0$, $\sigma_s = 0.05\ e.\mathrm{nm}^{-2}$. Black and magenta lines correspond to $\sigma = 0.1$ chains/nm^2 (PEL-modified nanopore) and $\sigma = 0$ chains/nm^2 (bare nanopore), respectively.

FIG. 10. Variation of the mean dimensionless magnetic field $\langle B^* \rangle$ versus (**a**) C_{KCl} and (**b**) pH for OEC (black lines) and ESC (blue lines) cases for fixed $\sigma = 0.1$ chains/nm^2, $\sigma_s = 0.05\ e.\mathrm{nm}^{-2}$ and $l_{\mathrm{slip}} = 0$.

FIG. 11. Advection and conduction contributions to the mean magnetic field, $\langle B^*_{\mathrm{str}} \rangle$ and $\langle B^*_{\mathrm{con}} \rangle$ (Eq. (41) with Eq. (48)) versus (**a**) C_{KCl} and (**b**) pH for OEC case while keeping the other parameters as $\sigma = 0.1$ chains/nm^2, $\sigma_s = 0.05\ e.\mathrm{nm}^{-2}$ and $l_{\mathrm{slip}} = 0$.

FIG. 12. Radial dependency of the dimensionless magnetic field $B^*(r)$ for (**a**,**b**) OEC case and (c,d) ESC case upon variation of (a,c) PEL grafting density at pH = 5, $C_{\mathrm{KCl}} = 0.01$ M and $\sigma_s = 0.05\ e.\mathrm{nm}^{-2}$ and (**b**,**d**) surface charge density pH = 1, $C_{\mathrm{KCl}} = 0.01$ M and $\sigma = 0.1$ chains/nm^2 for fixed $l_{\mathrm{slip}} = 0$. Black and magenta lines correspond to $\sigma = 0.1$ chains/nm^2 (PEL-modified nanopore) and $\sigma = 0$ chains/nm^2 (bare nanopore), respectively. The blue line in panel (d) corresponds to pH = 1, $C_{\mathrm{KCl}} = 1$ M, $\sigma = 0.6$ chains/nm^2, $\sigma_s = 0.05\ e.\mathrm{nm}^{-2}$, and $l_{\mathrm{slip}} = 0$ for degree of polymerization $N = 20$.

in the rest of the pore ($r < \approx 0.8$). This behavior is due to the fact that increasing C_{KCl} increases the net charge density and, at the same time, the EDL gets limited to an area close to the wall. Therefore, although the enhancement of ρ_e increases the flux of the ions, the thinning of the EDL and the lack of excess counterions in the central area of the nanopore leads to a decrease in the flux in the central areas, causing B^* to decrease in this region. In Fig. 9(b), the effect of pH on the magnetic field distribution is shown for the ESC case. By increasing pH from 1 to 3 the net flux of the ions is decreased due to the decrement of $\langle f \rangle$ and, consequently, of ρ_e. The decrease of the net flux of ions leads to decrease of B^* near the nanopore surface. However, because of the significant reduction in proton concentration, the thickness of the EDL increases, leading to higher B^* values away from the pore wall for pH = 3 than for pH = 1. This effect is more important when C_{KCl} is low. This is the main reason of the increasing trend of $\langle B^* \rangle$ at $C_{\mathrm{KCl}} = 0.001$, 0.01 and 0.1 M for low pH values for the ESC case shown in Fig. 10b, as well. On the other hand, by increasing the pH above 3, B^* decreases everywhere inside the pore because $\langle f \rangle$ decreases without any significant variation of the EDL thickness. The decreasing variation of $\langle B^* \rangle$ at high pH values shown in Fig. 10b for the ESC case follows the same explanation.

The radial distribution of magnetic field for different values of background salt concentration is shown in Fig. 9(c) for the OEC case. In this case, unlike the ESC mode, the reservoirs have different voltages and a streaming potential is induced due to the imbalance of the counterion concentrations at both ends of the nanochannel. The figure shows that increasing C_{KCl}, leads to negative B^* values. This behavior can be explained by the increase of the net charge density by increasing C_{KCl}. Although this effect may lead to a higher advection of the counterions in the positive z direction, it also enhances the electroosmotic advection and migration of counterions in the opposite direction, and, consequently, the interplay between both mechanisms determines the final trend. In this case, by increasing the salt concentration, the latter mechanism becomes dominant, which leads to the shift of B^* toward negative values. The decrease of $\langle B^* \rangle$ with C_{KCl} for the OSC case shown in Fig. 10(a) is also rooted in this fact. This conclusion is suported by Fig. 11(a), which shows that increasing C_{KCl} increases the contribution of the net ionic advection (superposition of the ionic advections due to purely pressure-driven flow and back electroomsotic flow) and enhances the contribution of the ionic migration.

In Fig. 9(d), the effect of pH on the distribution of B^* is presented. B^* turns positive when increasing the pH from 1 to 3. Increasing the pH above 3 leads to a decrease in the magnitude of B^*. This behavior can be interpreted as follows: when the pH varies from 1 to 3, the proton concentration is significantly decreased. Since protons have the highest electrical conductivity of all ions, the ionic migration in the negative direction is considerably diminished (especially at low C_{KCl})), leading to the dominance of ionic advection in the positive direction. This mechanism is backed by the contributions to the mean magnetic field shown in Fig. 11(b). This argument is also the reason of $\langle B^* \rangle$ becoming positive at low pH values at $C_{\mathrm{KCl}} = 0.001$ and 0.01 M in Fig. 10(b). Increasing the pH reduces ρ_e and, thus, decreases the contributions of the net ionic advection and migration (as shown in Fig. 11(b)). This effect leads to a reduction of B^* at pH = 5 and 8, see Fig. 9(d). Decreasing $\langle B^* \rangle$ with solution pH at pH > 3 in Fig. 10(b) is rooted in the mentioned reason as well. Moreover, the internal and external magnetic fields for a bare nanopore (nanopore having only surface charges) are shown in magenta lines in Fig. 9. When the degree of ionization of the polyelectrolyte layer is high, e.g., at low pHs and high background salt concentration, there is a drastic difference between the induced internal and external magnetic fields of a bare solid-state nanopore and a PEL-modified nanopore. This figure shows an important conclusion of this work: it is possible to enhance the internal magnetic fields by a factor > 10 by grafting polyelectrolyte brushes inside solid-state nanochannels. However, it should be noted that for alkaline pHs, e.g. pH = 8, where the degree of ionization is almost zero, there is no significative difference in the internal magnetic field between the PEL-modified and the bare nanochannels, see Fig. 9(b).

The effect of increasing σ and σ_s is shown in Fig. 12. The surface charge density was varied between zero charge and the typical surface charges observed for thiol self-assembled monolayers and metal oxide surfaces.[75] Increasing σ or σ_s increases ρ_e. This leads to the amplification of the ionic advection due to pressure-driven flow, and consequently, strengths

the internal and external magnetic fields. Furthermore, as it is visible in the Figure, there is a significant improvement in the induced internal and external magnetic fields inside a PEL-modified nanopore compared with the bare one.

Two prospective applications can be envisioned from the significant amplification of the magnetic field through the use of PE brushes. First, magnetic fields can be used as a secondary signature (in addition to the blockage of electric currents) to enhance the readout process in nanopore sensing technique. By applying a moderate pressure difference of 1 bar[16] between two ends of a pore with 1 μm length, we calculate a magnetic filed strength of ≈ 0.375 nT near the solid-surface under the conditions of the dashed-dotted line in Fig. 12(d). Upon increasing the surface grafting density, degree of polymerization, surface charge density, pressure gradient or reducing the pore legth, it is possible to obtain significantly higher magnetic field strengths. For example, the magnetic field distribution for a degree of polymerization $N = 20$ and a surface grafting density $\sigma = 0.6$ chains/nm^2 is shown (blue line) in Fig. 12(d). This curve exhibits a strong improvement of the magnetic field strength compared to the other results discussed so far (note, however, that those previous results used the values listed in Table I, for which we showed that the assumptions our theoretical framework are valid, see discussion above)

It was shown that magnetic fields as small as pico Tesla, which is less than the values reported here, can be sensed and measured in voltage/pressure driven electrokinetic flow in nanopores.[76–78] The sensitivity can be further extended to the order of femto Tesla in superconducting quantum interference device for detecting magnetic activity in the brain and heart of humans.[79,80]

An even more interesting application would be the detection of analyte translocation through nanopores in the absence of electrodes. In such type of non-invasive "wireless" nanochannel detectors, external magnetic fields can provide information on pressure-driven streaming currents and reveal translocation events without the need of placing external electrodes. A second application that can be envisaged is using PEL-modified nanochannels as management tools for displacing and adjusting the route of transport of biomolecules and particles that have an induced magnetic dipole in the working environment. In fact, due to the inhomogeneous magnetic field induced by the ionic flow, a magnetic force will be exerted on a translocating magnetic particle. Depending on the particle's trajectory in the nanochannel, this force can be used to displace the particle to a preferred radial location and make it subjected to the local axial flow velocity.[81]

IV. Conclusions

Despite the extensive use of ionic current measurements in nanopores functionalized with polymer brushes, it is still necessary to improve the theoretical frameworks for modeling the polymer brushes in these applications. A major opportunity for improvement stems from the fact that in most previous studies the electrostatic interactions were not obtained from minimizing the free energy of the system, and hence they did not reflect the effect of the brush configuration and excluded volume interactions. As a consequence, these previous studies needed to rely on simplified assumptions of constant height and uniform monomer distribution (or equivalently, a uniform charge distribution) within the polymer brushes.[82–88] The molecular approach we adopted here does not require such assumptions and, thus, captures the configurational preferences of the grafted polyeletrolyte brushes.

In this paper we explored a purely pressure-driven flow inside a pH-tunable polyelectrolyte grafted nanopore. The equilibrium structure of the system was determined with a mean field approach (molecular theory) and used as an input to determine non-equilibrium transport properties. The molecular theory is based on writing the total free energy of the system and then finding its extremum in the presence of the proper constraints. The extremum of the free energy obtained in this way corresponds to the equilibrium state of the system. This theory is a more rigorous description of the PE brushes than those used in previous works and provides us with molecular details that cannot be captured using the PNP and PB approaches, which were extensively used in previous studies. For example the molecular theory predicts the local distribution and state of ionization of the PE monomers and the local hydrodynamic frictional coefficient without assuming a priori a constant thickness of the PEL. Our results show that the highest electrokinetic-energy conversion efficiency occurs at mildly acidic pHs (pH = 4-5, for the value of pKa = 5.2 used in this work) and low salt concentrations. Moreover, it is shown that increasing the slip coefficient or the polymer grafting density does not necessarily lead to a higher efficiency. We showed that grafting pH-tunable polyelectrolyte brushes inside solid-state nanopores allows the induced magnetic field to be tuned by the environmental properties and can also drastically increase it even by multi ten factors. This strategy may enable in the future the application of magnetic fields for either enhancing the readout process in nanopore sensing techniques or as a management tool for controlling the route of translocation of magnetic analytes. Our approach can be also applied in the future to investigate nanopores coated by semi-flexible polymers by giving the bending and torsion potentials under different tethering and confinement conditions, and also to longer polymers than those studied here at a moderately increased computational cost.

Acknowledgements

M.S. and M.H.S. would like to acknowledge the financial support by the Iran's National Elites Foundation.

Data Availability Statement

The data that support the findings of this study are available from the corresponding author upon reasonable request.

Conflicts of interest

There are no conflicts to declare.

A. Special analytical solutions

In this section, four analytical solutions at low values of electrical potential field using the mean-field approach of Poisson-Boltzmann are obtained. The equations involve the Debye length, $\lambda_D = (k_B T \varepsilon_f / 2e^2 q_E^2 N_A C_0^{\text{bulk}})^{1/2}$, a parameter

FIG. 13. Variation of the modified Bessel functions of the first kind, $I_n(x)$, and the second kind, $K_n(x)$, versus x for $n \in \{0,1\}$. These functions control the asymptotic behaviors of analytic results such as Eqs. (A11), (A15) and (A16) i.e., $I_0(x) = 1 + x^2/4 + \mathcal{O}(x^2)$, $I_1(x) = x/2 + \mathcal{O}(x^2)$, $K_0(x) = (8x - 1 + \mathcal{O}(x^2))\Xi(x)$ and $K_1(x) = (3 + 8x + \mathcal{O}(x^2))\Xi(x)$ with $\Xi(x) = \sqrt{\pi/2}e^{-x}/(4x)^{3/2}$.

that characterizes the EDL thickness. Here, $q_E = |q_i^*| = 1$ because all the ions considered have the same $|q_i^*| = 1$, and $C_0^{\text{bulk}} = C_{K^+}^{\text{bulk}} + C_{H^+}^{\text{bulk}} = C_{Cl^-}^{\text{bulk}} + C_{OH^-}^{\text{bulk}}$. Results will be characterized by the dimensionless Debye–Hückel parameter

$$K = \frac{R_{\text{pore}}}{\lambda_D} \tag{A1}$$

which depends on the concentration of the ions and should vary over a limited range beyond $K > 1$ for the physically relevant situations we are addressing in this work. Upon varying either pH (which is equivalent to changing the H^+ ions concentration) or C_{KCl}, K consequently changes. The relation between pH, C_{KCl} and K is a combination of λ_D and the values of C_0^{bulk} reported below Eq. (16) in terms of pH and C_{KCl}.

1. Solid-State nanopore

By considering the Boltzmann distribution of the ions and using the Debye–Hückel approximation, the linearized Poisson-Boltzmann equation is reached as

$$\frac{1}{R}\frac{d}{dR}\left(R\frac{d\Psi}{dR}\right) = \lambda_D^{-2}\Psi \tag{A2}$$

Introducing additional dimensionless parameters

$$\psi_0 = \frac{k_B T}{e q_E}, \quad \psi = \frac{\Psi}{\psi_0} \tag{A3}$$

Eq. (A2) simplifies to

$$\frac{1}{r}\frac{d}{dr}\left(r\frac{d\psi}{dr}\right) = K^2\psi \tag{A4}$$

The solution of Eq. (A4) subject to the boundary conditions brought in Eq. (17), which involve the surface charge density σ_s^*, is given by

$$\psi(r) = \frac{\sigma_s^*}{K\varepsilon_f I_1(K)} I_0(Kr) \tag{A5}$$

where I_n is the nth modified Bessel function of the first kind (Fig. 13) and K is the dimensionless Debye–Hückel parameter. As mentioned previously, to evaluate the streaming current as well as the induced magnetic field, we need to find the velocity distribution. First, we start with the case of ESC model.

a. External short-circuited (ESC) mode

In this case, the momentum equation can be written as

$$\frac{\mu}{R}\frac{\partial}{\partial R}\left(R\frac{\partial U_z}{\partial R}\right) - \frac{dP}{dZ} = 0 \tag{A6}$$

or alternatively, in dimensionless form using Eqs. (10) and (19), as

$$\frac{1}{r}\frac{\partial}{\partial r}\left(r\frac{\partial u}{\partial r}\right) = 1 \tag{A7}$$

Through applying the boundary conditions (21) involving the dimensionless slip length l_{slip}, the resulting velocity field is obtained,

$$u(r) = -\left(\frac{1-r^2}{4} + \frac{l_{\text{slip}}}{2}\right) \tag{A8}$$

With the velocity field at hand, the streaming current is calculated via

$$I_{\text{str}} = \int_0^{R_{\text{pore}}} \rho_e(R) U_z(R) 2\pi R dR = I_{0,\text{str}} i_{\text{str}} \tag{A9}$$

where the previously defined $\rho_e(r)$ and $I_{0,\text{str}}$ are now expressed in terms of ρ_0^{bulk} instead of v_w, more specifically, $\rho_e(r) = \sum_{i\in\{\text{ions}\}} \rho_i = -2\rho_0^{\text{bulk}}\psi(r)$, and $I_{0,\text{str}} = -4\pi\rho_0^{\text{bulk}} e U_0 R_{\text{pore}}^2$. The dimensionless streaming current i_{str} inferred from Eq. (A9) can be evaluated analytically,

$$i_{\text{str}} = \int_0^1 u(r)\psi(r) r dr = \frac{A(K)}{4}\left[\frac{4I_1(K) - 2KI_0(K)}{K^3} - \frac{2l_{\text{slip}} I_1(K)}{K}\right] \tag{A10}$$

with a positive coefficient

$$A(K) = \frac{\sigma_s^*}{K\varepsilon_f I_1(K)} \tag{A11}$$

because we have considered positive surface charges, and the dimensionless magnetic field evaluates to

$$B^*(r) = \frac{B(r)}{B_0} = \frac{\int_0^r u(r)\psi(r) r dr}{r} = \frac{A(K)}{4}\left[\frac{4I_1(Kr) - 2KrI_0(Kr)}{K^3} - \frac{(2l_{\text{slip}} + 1 - r^2) I_1(Kr)}{K}\right] \tag{A12}$$

inside the nanopore ($0 < r \leq 1$) and

$$B^*(r) = \frac{i_{\text{str}}}{r} = \frac{A(K)}{4r}\left[\frac{4I_1(K) - 2KI_0(K)}{K^3} - \frac{2l_{\text{slip}} I_1(K)}{K}\right] \tag{A13}$$

outside the nanopore ($r \geq 1$), where $B_0 = -2\mu_p\rho_0^{\text{bulk}} e U_0 R_{\text{pore}}$ now also expressed in terms of ρ_0^{bulk}. $B^*(r)$ can both increase or decrease with r and exhibit either sign. There is a wide discussion on the behavior of $B^*(r)$ for different values of environment properties in section III.

b. Open external circuit (OEC) mode

In this case, through using the previous defined dimensionless parameters and applying the Debye-Hückel approximation, the momentum equation can be simplified as the following

$$\frac{1}{r}\frac{\partial}{\partial r}\left(r\frac{\partial u}{\partial r}\right) = 1 - \psi E_{\text{str}}^* \tag{A14}$$

where $E^*_{str} = E_{str}/E_0$ and $E_0 = -(dP/dZ)/2\rho_0^{bulk}e$ in terms of ρ_0^{bulk}. One can obtain the general solutions of Eq. (A14) satisfying the boundary conditions (21) as below

$$u(r) = -\left(\frac{1-r^2}{4} + \frac{l_{slip}}{2}\right) + \frac{AE^*_{str}}{K}\left[\frac{I_0(K) - I_0(Kr)}{K} + l_{slip}I_1(K)\right] \tag{A15}$$

with $A = A(K)$ from Eq. (A11). The streaming current $I_{str} = I_{str,P} + I_{str,E}$ through the nanopore is evaluated using (33) with the definition of $\rho_e(r) = -2\rho_0^{bulk}\psi(r)$ and the contributions u_P and u_E to the velocity field contained in Eq. (A15). The exact analytic result is $i_{str,P} = X_P$ and $i_{str,E} = X_E E^*_{str}$, with X_P and X_E defined by Eqs. (34) and (35),

$$X_P = \frac{A}{4K^3}\left[4I_1(K) - 2KI_0(K) - 2l_{slip}K^2I_1(K)\right], \tag{A16}$$

$$X_E = \frac{A^2}{2K^3}\left\{[2I_1(K) - KI_0(K)]I_0(K) + (1+2l_{slip})KI_1^2(K)\right\} \tag{A17}$$

The streaming potential also induces a dimensionless conduction current $i_{con} = X_{con}E^*_{str}$ through the nanochannel, which can be calculated analytically using Eq. (36) and $C_i = C_i^{bulk}\exp(-q_i^*\psi) = C_i^{bulk}(1 - q_i^*\psi)$. We obtain

$$\begin{aligned} X_{con} &= \frac{2\pi E_0 R^2_{pore}}{I_{0,str}} \sum_{i\in\{ions\}} \left(\frac{1}{2} - q_i^* \int_0^1 \psi r dr\right) \lambda_i C_i^{bulk} \\ &= \frac{2\pi E_0 R^2_{pore}}{I_{0,str}} \sum_{i\in\{ions\}} \left(\frac{1}{2} - \frac{AI_1(K)q_i^*}{K}\right) \lambda_i C_i^{bulk} \end{aligned} \tag{A18}$$

In the steady-state, the net ionic current vanishes, that is $I_{str,P} + I_{str,E} + I_{con} = 0$. Therefore, the streaming potential, E^*_{str} as function of K is given by Eq. (38) with X_P, X_E and X_{con} now available from Eqs. (A16)–(A18). Having evaluated E^*_{str}, the velocity profile is explicitly given by Eq. (A15) and the dimensionless streaming current is determined by $i_{str} = X_E E^*_{str} + X_P$.

Finally, by using the Ampere's law, the induced magnetic field inside the nanopore can be calculated,

$$\begin{aligned} B^*(r) = {} & \frac{A}{4K^3}\left\{[4 - K^2(2l_{slip} + 1 - r^2)]I_1(Kr) - 2KrI_0(K)\right\} \\ & + \frac{E^*_{str}A^2}{2K^3}\left\{Kr[I_1^2(Kr) - I_0^2(Kr)] + 2[Kl_{slip}I_1(K) + I_0(K)]I_1(Kr)\right\} \\ & + \frac{E_{str}\mu_p R_{pore}}{B_0} \sum_{i\in\{ions\}} \left(\frac{r^2}{2} - \frac{AI_1(Kr)q_i^*}{K}\right) \lambda_i C_i^{bulk} \end{aligned} \tag{A19}$$

where $A = A(K)$ is given in Eq. (A11) and B_0 stated after Eq. (A13).

2. Soft nanopore

For soft nanopore, the Poisson-Boltzmann equation at low potential values can be written as

$$\frac{1}{R}\frac{d}{dR}\left(R\frac{d\Psi_{PEL}}{dR}\right) = 2\frac{e^2q_E^2N_AC_0^{bulk}}{k_BT\varepsilon_f}\Psi_{PEL} + \frac{e\rho_{PEL}}{\varepsilon_f} \tag{A20}$$

inside the polyelectrolyte layer (PEL), i.e., for $R_{pore} - \delta_s \le R \le R_{pore}$, and

$$\frac{1}{R}\frac{d}{dR}\left(R\frac{d\Psi_E}{dR}\right) = 2\frac{e^2q_E^2N_AC_0^{bulk}}{k_BT\varepsilon_f}\Psi \tag{A21}$$

in the solution outside the PEL, $0 \le R \le R_{pore} - \delta_s$. Here, ρ_{PEL} refers to the fixed PEL charge density, R_{pore} shows the nanopore radius and δ_s represents the constant thickness of the PEL layer. The subscripts PEL and E indicate inside and outside regions of the the polyelectrolyte layer, respectively. By using the dimensionless parameters defined in previous section and the new ones defined as

$$\lambda_{PEL} = \left(\frac{k_BT\varepsilon_f}{\rho_{PEL}e^2}\right)^{1/2}, \qquad \Lambda = \frac{\lambda_D}{\lambda_{PEL}}, \qquad \delta_s^* = \frac{\delta_s}{R_{pore}} \tag{A22}$$

as well as the dimensionless void radius,

$$r_b = 1 - \delta_s^* \tag{A23}$$

Equations (A20) and (A21) are non-dimensionalized as

$$\begin{aligned} 0 &= \frac{1}{r}\frac{d}{dr}\left(r\frac{d\psi_{PEL}}{dr}\right) - K^2\left(\psi_{PEL} - \Lambda^2\right) \quad (r_b \le r \le 1) \\ 0 &= \frac{1}{r}\frac{d}{dr}\left(r\frac{d\psi_E}{dr}\right) - K^2\psi_E \qquad (0 \le r \le 1 - r_b) \end{aligned} \tag{A24}$$

with the pertinent boundary conditions $\psi'_E(0) = 0$, $\psi'_E(r_b) = \psi'_{PEL}(r_b)$, $\psi_E(r_b) = \psi_{PEL}(r_b)$, and $\psi'_{PEL}(1) = \sigma_s^*$, where the prime denotes a derivative with respect to r. For the general solutions of Eq. (A24) we obtain

$$\psi_{PEL}(r) = \Lambda^2 + c_1I_0(Kr) + c_2K_0(Kr), \tag{A25}$$

$$\psi_E(r) = c_3I_0(Kr) + c_4K_0(Kr) \tag{A26}$$

where K_n is the nth modified Bessel function of the second kind (Fig. 13). The coefficients c_1–c_4 are obtained upon satisfying the stated boundary conditions,

$$\begin{aligned} c_1 &= \frac{\sigma_s^*}{\varepsilon_f KI_1(K)} + \frac{c_2K_1(K)}{I_1(K)}, \\ c_2 &= -\frac{\Lambda^2I_1(Kr_b)}{K_0(Kr_b)I_1(Kr_b) + K_1(Kr_b)I_0(Kr_b)}, \\ c_3 &= \frac{\sigma_s^*}{\varepsilon_f KI_1(K)} - \frac{\Lambda^2[K_1(K)I_1(Kr_b) - K_1(Kr_b)I_1(K)]}{I_1(K)[K_0(Kr_b)I_1(Kr_b) + K_1(Kr_b)I_0(Kr_b)]}, \\ c_4 &= 0 \end{aligned} \tag{A27}$$

To evaluate the streaming current as well as the induced magnetic fields, we need to find the velocity distribution. We begin with the case of the ESC mode.

a. *External short-circuited (ESC) mode*

By modeling PEL as a porous medium and utilizing the Brinkman equation, the momentum equation can be simplified as the following wherein the drag force is accounted by a volumetric resistive force proportional to the velocity, that is

$$\frac{\mu}{R}\frac{\partial}{\partial R}\left(R\frac{\partial U_z}{\partial R}\right) - hF_*U_z - \frac{dP}{dZ} = 0 \tag{A28}$$

where F_* is the constant hydrodynamic frictional coefficient of the PEL and h is equal to 1 inside the grafted layer and

zero within the electrolyte. By using the previous dimensionless variables and defining the dimensionless hydrodynamic frictional coefficient

$$f_* = R_{\text{pore}}\sqrt{\frac{F_*}{\mu}} \tag{A29}$$

the momentum equation can be scaled as

$$1 = \frac{1}{r}\frac{\partial}{\partial r}\left(r\frac{\partial u_{\text{PEL}}}{\partial r}\right) - f_*^2 u_{\text{PEL}}, \quad (r_b \le r \le 1), \tag{A30}$$

$$1 = \frac{1}{r}\frac{\partial}{\partial r}\left(r\frac{\partial u_E}{\partial r}\right) \qquad (0 \le r \le r_b) \tag{A31}$$

The momentum equation is subject to symmetry and continuity at the soft layer interface and slip boundary conditions at the wall, these all are written in dimensionless form as $u_E'(0) = 0$, $u_E'(r_b) = u_{\text{PEL}}'(r_b)$, $u_E(r_b) = u_{\text{PEL}}(r_b)$, and $u_{\text{PEL}}(1) = -l_{\text{slip}}u_{\text{PEL}}'(1)$. The solution of Eqs. (A30) and (A31) satisfying these pertinent boundary conditions may be expressed as

$$u_{\text{PEL}}(r) = c_1^{\text{vel}} I_0(f_* r) + c_2^{\text{vel}} K_0(f_* r) - \frac{1}{f_*^2}, \tag{A32}$$

$$u_E(r) = \frac{r^2 - r_b^2}{4} + c_3^{\text{vel}} \ln(r) + c_4^{\text{vel}} - \frac{1}{f_*^2} \tag{A33}$$

where the c^{vel} coefficients are given, with the help of abbreviations

$$\gamma_1 = K_0(f_*) - l_{\text{slip}} f_* K_1(f_*), \tag{A34}$$

$$\gamma_2 = I_0(f_*) + l_{\text{slip}} f_* I_1(f_*) \tag{A35}$$

by

$$\begin{aligned} c_1^{\text{vel}} &= \frac{r_b}{2 f_* I_1(f_* r_b)} + \frac{c_2^{\text{vel}} K_1(f_* r_b)}{I_1(f_* r_b)}, \\ c_2^{\text{vel}} &= \frac{I_1(f_* r_b)/f_*^2 - r_b \gamma_2/2 f_*}{\gamma_1 I_1(f_* r_b) + \gamma_2 K_1(f_* r_b)} \\ c_3^{\text{vel}} &= 0, \\ c_4^{\text{vel}} &= c_1^{\text{vel}} I_0(f_* r_b) + c_2^{\text{vel}} K_0(f_* r_b) \end{aligned} \tag{A36}$$

Now the dimensionless streaming current is found as

$$\begin{aligned} i_{\text{str}} &= \int_0^1 u(r)\psi(r) r dr \\ &= \int_{r_b}^1 \psi_{\text{PEL}}(r) u_{\text{PEL}}(r) r dr + \frac{c_3 c_4^{\text{vel}} r_b I_1(K r_b)}{K} \\ &\quad + \frac{c_3 r_b}{4K^3}\left[\left(4 + K^2 r_b^2\right) I_1(K r_b) - 2K r_b I_0(K r_b)\right] \end{aligned} \tag{A37}$$

where $\psi_{\text{PEL}}(r)$, $u_{\text{PEL}}(r)$ and the c coefficients are specified by Eqs. (A25), (A27), (A32), and (A36), and we recall $r_b = 1 - \delta_s^* = 1 - \delta_s/R_{\text{pore}}$.

Through using the Ampere's law in a closed circular loop of radius r written in Eq. (24), we can find the dimensionless magnetic field defined previously as

$$B^*(r) = \frac{c_3}{4K^3}\left[\left(4 + K^2 r^2\right) I_1(Kr) - 2Kr I_0(Kr)\right] + \frac{c_3 c_4^{\text{vel}} I_1(Kr)}{K} \tag{A38}$$

for $0 \le r \le r_b$ and

$$B^*(r) = \frac{1}{r}\left[\int_{r_b}^r \psi_{\text{PEL}}(r) u_{\text{PEL}}(r) r dr + r_b B^*(r_b)\right] \tag{A39}$$

for $r_b \le r \le 1$, where $B^*(r_b)$ is the magnitude of dimensionless magnetic field at $r = r_b$ obtained from Eq. (A38). Also, for the outside magnetic field, one can obtain

$$B^*(r) = \frac{B^*(1)}{r} = \frac{i_{\text{str}}}{r} \tag{A40}$$

where $B^*(1)$ is the value of the dimensionless magnetic field at $r = 1$ evaluated from Eq. (A39).

b. Open external circuit (OEC) mode

In this case, due to the imbalance of ions distribution at the inlet and outlet of the nanochannel, caused by the imposed pressure gradient, an electrical potential E_{str} is induced. The momentum equation is rewritten in dimensionless form as the following

$$\begin{aligned} \frac{1}{r}\frac{\partial}{\partial r}\left(r\frac{\partial u_{\text{PEL}}}{\partial r}\right) - f_*^2 u_{\text{PEL}} &= 1 - \psi_{\text{PEL}} E_{\text{str}}^*, \quad (r_b \le r \le 1), \\ \frac{1}{r}\frac{\partial}{\partial r}\left(r\frac{\partial u_E}{\partial r}\right) &= 1 - \psi_E E_{\text{str}}^*, \quad (0 \le r \le r_b) \end{aligned} \tag{A41}$$

where E_{str}^* had been defined previously. The general solutions of Eqs. (A41) are obtained as

$$\begin{aligned} u_{\text{PEL}}(r) = \frac{E_{\text{str}}^* \Lambda^2 - 1}{f_*^2} + \frac{c_1 E_{\text{str}}^* I_0(Kr) + c_2 E_{\text{str}}^* K_0(Kr)}{f_*^2 - K^2} \\ + C_1^{\text{vel}} I_0(f_* r) + C_2^{\text{vel}} K_0(f_* r) \end{aligned} \tag{A42}$$

inside the PEL ($r_b \le r \le 1$), and

$$u_E(r) = \frac{r^2}{4} - \frac{c_3 E_{\text{str}}^* I_0(Kr)}{2} + C_3^{\text{vel}} \ln(r) + C_4^{\text{vel}} \tag{A43}$$

outside the PEL ($0 \le r \le r_b$). By satisfying the boundary conditions stated after Eq. (A31), the four yet unknown parameters can be found as $C_1^{\text{vel}} = L_1 + L_2 E_{\text{str}}^*$, $C_2^{\text{vel}} = L_3 + L_4 E_{\text{str}}^*$, $C_3^{\text{vel}} = 0$, and $C_4^{\text{vel}} = L_6 + L_5 E_{\text{str}}^*$ with

$$\begin{aligned} L_1 &= \frac{\gamma_1 r_b/2 + K_1(f_* r_b)/f_*}{f_*\left[\gamma_1 I_1(f_* r_b) + \gamma_2 K_1(f_* r_b)\right]}, \\ L_2 &= \frac{\gamma_1 \gamma_4 - f_* \gamma_3 K_1(f_* r_b)}{f_*\left[\gamma_1 I_1(f_* r_b) + \gamma_2 K_1(f_* r_b)\right]}, \\ L_3 &= \frac{f_*^{-2} - L_1 \gamma_2}{\gamma_1}, \\ L_4 &= -\frac{\gamma_3 + L_2 \gamma_2}{\gamma_1}, \\ L_5 &= \frac{\Lambda^2}{f_*^2} + \frac{c_1 I_0(Kr_b) + c_2 K_0(Kr_b)}{f_*^2 - K^2} + \frac{c_3 I_0(Kr_b)}{K^2} \\ &\quad + L_2 I_0(f_* r_b) + L_4 K_0(f_* r_b), \\ L_6 &= -\frac{1}{f_*^2} - \frac{r_b^2}{4} + L_1 I_0(f_* r_b) + L_3 K_0(f_* r_b), \end{aligned} \tag{A44}$$

with c_1, c_2, c_3 defined in Eq. (A27), K, Λ, r_b and f_* in Eqs. (A1), (A22), (A23), and (A29), and

$$\gamma_3 = \frac{\Lambda^2}{f_*^2} + \frac{c_1 I_0(K) + c_2 K_0(K)}{f_*^2 - K^2} + \frac{K l_{\text{slip}}[c_1 I_1(K) - c_2 K_1(K)]}{f_*^2 - K^2},$$
$$\gamma_4 = -\frac{c_3 I_1(K r_b)}{K} + \frac{c_2 K K_1(K r_b) - c_1 K I_1(K r_b)}{f_*^2 - K^2} \quad \text{(A45)}$$

while γ_1 and γ_2 had already been defined by Eqs. (A34) and (A35). By substitution of Eqs. (A44)–(A45) into Eq. (A43), one obtains

$$u_{\text{PEL}}(r) = E_{\text{str}}^* \left[\frac{\Lambda^2}{f_*^2} + \frac{c_1 I_0(Kr) + c_2 K_0(Kr)}{f_*^2 - K^2} + L_2 I_0(f_* r) + L_4 K_0(f_* r) \right.$$
$$\left. + L_1 I_0(f_* r) + L_3 K_0(f_* r) - \frac{1}{f_*^2} \right] \qquad (r_b \le r \le 1) \quad \text{(A46)}$$
$$u_E(r) = \frac{r^2}{4} + L_6 + E_{\text{str}}^* \left[L_5 - \frac{c_3 I_0(Kr)}{K^2} \right] \qquad (0 \le r \le r_b) \quad \text{(A47)}$$

Equations (A46)-(A47) imply that the fluid velocity highly depends on both the induced steaming potential as well as the imposed pressure gradient. The streaming current through the nanopore can be exactly evaluated using Eqs. (33)–(35) with the following values for X_P and X_E

$$X_P = \int_{r_b}^1 \psi_{\text{PEL}}(r) \left[L_1 I_0(f_* r) + L_3 K_0(f_* r) - \frac{1}{f_*^2} \right] r dr$$
$$+ \frac{c_3 r_b}{4K^3} \left[(4 + K^2 r_b^2) I_1(K r_b) - 2K r_b I_0(K r_b) \right] + \frac{c_3 L_6 r_b I_1(K r_b)}{K}$$
$$X_E = \frac{\Lambda^2}{f_*^2} \int_{r_b}^1 \psi_{\text{PEL}}(r) r dr$$
$$+ \int_{r_b}^1 \psi_{\text{PEL}}(r) \left[\frac{c_1 I_0(Kr) + c_2 K_0(Kr)}{f_*^2 - K^2} + L_2 I_0(f_* r) + L_4 K_0(f_* r) \right] r dr$$
$$+ \frac{c_3 L_5 r_b I_1(K r_b)}{K} - \frac{c_3^2 r_b^2}{2K^2} \left[I_0^2(K r_b) - I_1^2(K r_b) \right]$$

with $\psi_{\text{PEL}}(r)$ from Eq. (A25). The streaming potential also induces a conduction current through the nanochannel, calculated by Eq. (36) with the below value for X_{con}

$$X_{\text{con}} = \frac{2\pi E_0 R_{\text{pore}}^2}{I_{0,\text{str}}} \sum_{i \in \{\text{ions}\}} \left(\frac{1}{2} - L_7 q_i^* \right) \lambda_i C_i^{\text{bulk}} \quad \text{(A49)}$$

with

$$L_7 = \frac{\Lambda^2 (1 - r_b^2)}{2} + \frac{c_3 r_b I_1(K r b)}{K}$$
$$+ \frac{c_1 [I_1(K) - r_b I_1(K r_b)] - c_2 [K_1(K) - r_b K_1(K r_b)]}{K} \quad \text{(A50)}$$

Now the values of E_{str}^* can be evaluated using Eq. (38) and $i_{\text{str}} = X_E E_{\text{str}}^* + X_P$. Finally, by using the Ampere's law, the induced magnetic field inside the nanopore can be calculated as

$$B^*(r) = \frac{c_3}{4K^3} \left[(4 + K^2 r^2) I_1(Kr) - 2Kr I_0(Kr) \right] + \frac{c_3 L_6}{K} I_1(Kr)$$
$$+ E_{\text{str}}^* \left[\frac{c_3 L_5 I_1(Kr)}{K} - \frac{c_3^2 r^2}{2K^2} \left\{ I_0^2(Kr) - I_1^2(Kr) \right\} \right]$$
$$+ \frac{E_0 \mu_p R_{\text{pore}}}{B_0} E_{\text{str}}^* \sum_{i \in \{\text{ions}\}} \left[\frac{r}{2} - \frac{c_3 I_1(Kr) q_i^*}{K} \right] \lambda_i C_i^{\text{bulk}} \quad \text{(A51)}$$

for $0 \le r \le r_b$ and

$$B^*(r) = \frac{1}{r} \left[\frac{E_{\text{str}} R_{\text{pore}}}{B_0} \sum_{i \in \{\text{ions}\}} \left(\frac{r^2 - r_b^2}{2} - q_i^* \int_{r_b}^r \psi_{\text{PEL}}(r) r dr \right) \lambda_i C_i^{\text{bulk}} \right]$$
$$+ r_b B^*(r_b) + \int_{r_b}^r \psi_{\text{PEL}}(r) u_{\text{PEL}}(r) r dr \quad \text{(A52)}$$

for $r_b \le r \le 1$, while $B_0 = -2\mu_p \rho_0^{\text{bulk}} e U_0 R_{\text{pore}}$, ψ_{PEL} and u_{PEL} are given by Eqs. (A25) and (A46), respectively.

[1] H. Bayley and P. S. Cremer. Stochastic sensors inspired by biology. *Nature*, 413:226–230, 2001.
[2] Charles R. Martin and Zuzanna S. Siwy. Learning nature's way: Biosensing with synthetic nanopores. *Science*, 317:331–332, 2007.
[3] Lindsay T. Sexton, Lloyd P. Horne, Stefanie A. Sherrill, Gregory W. Bishop, Lane A. Baker, and Charles R. Martin. Resistive-pulse studies of proteins and protein/antibody complexes using a conical nanotube sensor. *J. Amer. Chem. Soc.*, 129:13144–13152, 2007.
[4] Todd C. Sutherland, Yi-Tao Long, Radu-Ioan Stefureac, Irene Bediako-Amoa, Heinz-Bernhard Kraatz, and Jeremy S. Lee. Structure of peptides investigated by nanopore analysis. *Nano Lett.*, 4:1273–1277, 2004.
[5] Basit Yameen, Mubarak Ali, Reinhard Neumann, Wolfgang Ensinger, Wolfgang Knoll, and Omar Azzaroni. Synthetic proton-gated ion channels via single solid-state nanochannels modified with responsive polymer brushes. *Nano Lett.*, 9:2788–2793, 2009.
[6] Basit Yameen, Mubarak Ali, Reinhard Neumann, Wolfgang Ensinger, Wolfgang Knoll, and Omar Azzaroni. Ionic transport through single solid-state nanopores controlled with thermally nanoactuated macromolecular gates. *Small*, 5:1287–1291, 2009.
[7] Mubarak Ali, Patricio Ramirez, Saima Nasir, Javier Cervera, Salvador Mafe, and Wolfgang Ensinger. Ionic circuitry with nanofluidic diodes. *Soft Matter*, 15:9682–9689, 2019.
[8] Rohit Karnik, Chuanhua Duan, Kenneth Castelino, Hirofumi Daiguji, and Arun Majumdar. Rectification of ionic current in a nanofluidic diode. *Nano Lett.*, 7:547–551, 2007.
[9] Huang Dai, Yuqing Li, Yingchun Fu, and Yanbin Li. Enzyme catalysis induced polymer growth in nanochannels: A new approach to regulate ion transport and to study enzyme kinetics in nanospace. *Electroanal.*, 30:328–335, 2018.
[10] Wenhong Li, Nicholas A. W. Bell, Silvia Hernández-Ainsa, Vivek V. Thacker, Alana M. Thackray, Raymond Bujdoso, and Ulrich F. Keyser. Single protein molecule detection by glass nanopores. *ACS Nano*, 7:4129–4134, 2013.
[11] C. Liu, E. I. Gillette, X. Y. Chen, A. J. Pearse, A. C. Kozen, M. A. Schroederand K. E. Gregorczyk, S. B. Lee, and G. W. Rubloff. An all-in-one nanopore battery array. *Nat. Nanotechn.*, 9:1031–1039, 2014.
[12] Hirofumi Daiguji, Peidong Yang, Andrew J. Szeri, and Arun Majumdar. Electrochemomechanical energy conversion in nanofluidic channels. *Nano Lett.*, 4:2315–2321, 2004.
[13] Hengbin Zhang, Qing Zhao, Zhipeng Tang, Song Liu, Qingtao Li, Zhongchao Fan, Fuhua Yang, Liping You, Xuemei Li, Jingmin Zhang, and Dapeng Yu. Slowing down dna translocation through solid-state nanopores by pressure. *Small*, 9:4112–4117, 2013.
[14] David P. Hoogerheide, Bo Lu, and Jene A. Golovchenko. Pressure–voltage trap for dna near a solid-state nanopore. *ACS Nano*, 8:7384–7391, 2014.
[15] Wen-Jie Lan, Deric A. Holden, Jin Liu, and Henry S. White. Pressure-driven nanoparticle transport across glass membranes containing a conical-shaped nanopore. *J. Phys. Chem. C*, 115:18445–18452, 2011.

[16]Bo Lu, David P. Hoogerheide, Qing Zhao, Hengbin Zhang, Zhipeng Tang, Dapeng Yu, and Jene A. Golovchenko. Pressure-controlled motion of single polymers through solid-state nanopores. *Nano Lett.*, 13:3048–3052, 2013.

[17]Frank H. J. van der Heyden, Douwe Jan Bonthuis, Derek Stein, Christine Meyer, and Cees Dekker. Power generation by pressure-driven transport of ions in nanofluidic channels. *Nano Lett.*, 7:1022–1025, 2007.

[18]Frank H. J. van der Heyden, Douwe Jan Bonthuis, Derek Stein, Christine Meyer, and Cees Dekker. Electrokinetic energy conversion efficiency in nanofluidic channels. *Nano Lett.*, 6:2232–2237, 2006.

[19]Christian Davidson and Xiangchun Xuan. Electrokinetic energy conversion in slip nanochannels. *J. Power Sources*, 179:297–300, 2008.

[20]Reto B. Schoch, Harald van Lintel, and Philippe Renaud. Effect of the surface charge on ion transport through nanoslits. *Phys. Fluids*, 17:100604, 2005.

[21]Morteza Sadeghi, Mohammad Hassan Saidi, Ali Moosavi, and Arman Sadeghi. Geometry effect on electrokinetic flow and ionic conductance in ph-regulated nanochannels. *Phys. Fluids*, 29:122006, 2017.

[22]Morteza Sadeghi, Mohammad Hassan Saidi, and Arman Sadeghi. Electroosmotic flow and ionic conductance in a ph-regulated rectangular nanochannel. *Phys. Fluids*, 29:062002, 2017.

[23]Double layer overlap in ac electroosmosis. *Europ. J. Mech. B*, 27:297–308, 2008.

[24]Suguru Iwai, Taichi Suzuki, Hiroki Sakagami, Kazuhiro Miyamoto, Zhenghao Chen, Mariko Konishi, Elena Villani, Naoki Shida, Ikuyoshi Tomita, and Shinsuke Inagi. Electropolymerization without an electric power supply. *Commun. Chem.*, 5:66, 2022.

[25]A. Mansouri, P. Taheri, and L. W. Kostiuk. Streaming current magnetic fields in a charged nanopore. *Sci. Rep.*, 6:36771, 2016.

[26]G. Wilhelmina de Groot, M. Gabriella Santonicola, Kaori Sugihara, Tomaso Zambelli, Erik Reimhult, János Vörös, and G. Julius Vancso. Switching transport through nanopores with ph-responsive polymer brushes for controlled ion permeability. *ACS Appl. Mater. Interf.*, 5:1400–1407, 2013.

[27]Mubarak Ali, Basit Yameen, Reinhard Neumann, Wolfgang Ensinger, Wolfgang Knoll, and Omar Azzaroni. Biosensing and supramolecular bioconjugation in single conical polymer nanochannels. facile incorporation of biorecognition elements into nanoconfined geometries. *J. Amer. Chem. Soc.*, 130:16351–16357, 2008.

[28]Mubarak Ali, Basit Yameen, Javier Cervera, Patricio Ramírez, Reinhard Neumann, Wolfgang Ensinger, Wolfgang Knoll, and Omar Azzaroni. Layer-by-layer assembly of polyelectrolytes into ionic current rectifying solid-state nanopores: Insights from theory and experiment. *J. Amer. Chem. Soc.*, 132:8338–8348, 2010.

[29]Basit Yameen, Mubarak Ali, Reinhard Neumann, Wolfgang Ensinger, Wolfgang Knoll, and Omar Azzaroni. Single conical nanopores displaying ph-tunable rectifying characteristics. manipulating ionic transport with zwitterionic polymer brushes. *J. Amer. Chem. Soc.*, 131:2070–2071, 2009.

[30]Basit Yameen, Mubarak Ali, Reinhard Neumann, Wolfgang Ensinger, Wolfgang Knoll, and Omar Azzaroni. Proton -regulated rectified ionic transport through solid-state conical nanopores modified with phosphate-bearing polymer brushes. *Chem. Commun.*, 46:1908–1910, 2010.

[31]Antonio Alcaraz, Patricio Ramírez, Elena García-Giménez, M. Lidón López, Andreu Andrio, and Vicente M. Aguilella. A ph-tunable nanofluidic diode: Electrochemical rectification in a reconstituted single ion channel. *J. Phys. Chem. B*, 110:21205–21209, 2006.

[32]F. A. Morrison and J. F. Osterle. Electrokinetic energy conversion in ultrafine capillaries. *J. Chem. Phys.*, 43:2111–2115, 1965.

[33]R. J. Gross and J. F. Osterle. Membrane transport characteristics of ultrafine capillaries. *J. Chem. Phys.*, 49:228–234, 1968.

[34]D. Burgreen and F. R. Nakache. Electrokinetic flow in ultrafine capillary slits1. *J. Phys. Chem.*, 68:1084–1091, 1964.

[35]D. Burgreen and F. Nakache. Efficiency of pumping and power generation in ultrafine electrokinetic systems. *J. Appl. Mech.*, 32:675–679, 1965.

[36]Jun Yang, Fuzhi Lu, Larry W Kostiuk, and Daniel Y Kwok. Electrokinetic microchannel battery by means of electrokinetic and microfluidic phenomena. *J. Micromech. Microeng.*, 13:963–970, oct 2003.

[37]Chih-Chang Chang and Ruey-Jen Yang. Electrokinetic energy conversion efficiency in ion-selective nanopores. *Appl. Phys. Lett.*, 99:083102, 2011.

[38]Sofie Haldrup, Jacopo Catalano, Michael Ryan Hansen, Manfred Wagner, Grethe Vestergaard Jensen, Jan Skov Pedersen, and Anders Bentien. High electrokinetic energy conversion efficiency in charged nanoporous nitrocellulose/sulfonated polystyrene membranes. *Nano Lett.*, 15:1158–1165, 2015.

[39]Yongqiang Ren and Derek Stein. Slip-enhanced electrokinetic energy conversion in nanofluidic channels. *Nanotechn.*, 19:195707, apr 2008.

[40]Sourayon Chanda, Shayandev Sinha, and Siddhartha Das. Streaming potential and electroviscous effects in soft nanochannels: towards designing more efficient nanofluidic electrochemomechanical energy converters. *Soft Matter*, 10:7558–7568, 2014.

[41]Guang Chen and Siddhartha Das. Streaming potential and electroviscous effects in soft nanochannels beyond debye-huckel linearization. *J. Colloid Interf. Sci.*, 445:357–363, 2015.

[42]Yongjun Jian, Fengqin Li, Yongbo Liu, Long Chang, Quansheng Liu, and Liangui Yang. Electrokinetic energy conversion efficiency of viscoelastic fluids in a polyelectrolyte-grafted nanochannel. *Coll. Surf. B*, 156:405–413, 2017.

[43]J. Patwary, G. Chen, and S. Das. Efficient electrochemomechanical energy conversion in nanochannels grafted with polyelectrolyte layers with ph-dependent charge density. *Microfluid. Nanofluid.*, 20:37, 2016.

[44]Harnoor Singh Sachar, Vishal Sankar Sivasankar, and Siddhartha Das. Electrokinetic energy conversion in nanochannels grafted with ph-responsive polyelectrolyte brushes modelled using augmented strong stretching theory. *Soft Matter*, 15:5973–5986, 2019.

[45]Antarip Poddar, Debonil Maity, Aditya Bandopadhyay, and Suman Chakraborty. Electrokinetics in polyelectrolyte grafted nanofluidic channels modulated by the ion partitioning effect. *Soft Matter*, 12:5968–5978, 2016.

[46]Li-Hsien Yeh, Mingkan Zhang, and Shizhi Qian. Ion transport in a ph-regulated nanopore. *Analyt. Chem.*, 85:7527–7534, 2013.

[47]Zhenping Zeng, Li-Hsien Yeh, Mingkan Zhang, and Shizhi Qian. Ion transport and selectivity in biomimetic nanopores with ph-tunable zwitterionic polyelectrolyte brushes. *Nanoscale*, 7:17020–17029, 2015.

[48]Zhenping Zeng, Ye Ai, and Shizhi Qian. ph-regulated ionic current rectification in conical nanopores functionalized with polyelectrolyte brushes. *Phys. Chem. Chem. Phys.*, 16:2465–2474, 2014.

[49]Li-Hsien Yeh, Mingkan Zhang, Ning Hu, Sang W. Joo, Shizhi Qian, and Jyh-Ping Hsu. Electrokinetic ion and fluid transport in nanopores functionalized by polyelectrolyte brushes. *Nanoscale*, 4:5169–5177, 2012.

[50]Yu Ma, Li-Hsien Yeh, Chih-Yuan Lin, Lanju Mei, and Shizhi Qian. ph-regulated ionic conductance in a nanochannel with overlapped electric double layers. *Analyt. Chem.*, 87:4508–4514, 2015.

[51]Ming-Jiang Huang, Lanju Mei, Li-Hsien Yeh, and Shizhi Qian. ph-regulated nanopore conductance with overlapped electric double layers. *Electrochem. Commun.*, 55:60–63, 2015.

[52]M. Sadeghi, A. Sadeghi, and M. H. Saidi. Electroosmotic flow in hydrophobic microchannels of general cross section. *J. Fluid Eng.*, 138:031104, 2015.

[53]Ranabir Dey, Debapriya Chakraborty, and Suman Chakraborty. Analytical solution for thermally fully developed combined electroosmotic and pressure-driven flows in narrow confinements with thick electrical double layers. *J. Heat Transf. - Trans. ASME*, 133:024503, 2011.

[54]Orit Peleg, Mario Tagliazucchi, Martin Kröger, Yitzhak Rabin, and Igal Szleifer. Morphology control of hairy nanopores. *ACS Nano*, 5:4737–4747, 2011.

[55]Mario Tagliazucchi, Xing Li, Monica Olvera de la Cruz, and Igal Szleifer. Self-organized polyelectrolyte end-grafted layers under nanoconfinement. *ACS Nano*, 8:9998–10008, 2014.

[56]Yamila A. Perez Sirkin, Igal Szleifer, and Mario Tagliazucchi. Voltage-triggered structural switching of polyelectrolyte-modified nanochannels. *Macromolecules*, 53:2616–2626, 2020.

[57]Yamila A. Perez Sirkin, Mario Tagliazucchi, and Igal Szleifer. Nanopore gates via reversible crosslinking of polymer brushes: a theoretical study. *Soft Matter*, 17:2791–2802, 2021.

[58]Morteza Sadeghi, Mohammad Hassan Saidi, Ali Moosavi, and Martin Kröger. Tuning electrokinetic flow, ionic conductance, and selectivity in a solid-state nanopore modified with a ph-responsive polyelectrolyte brush: A molecular theory approach. *J. Phys. Chem. C*, 124:18513–18531, 2020.

[59]Mario Tagliazucchi and Igal Szleifer. Routes for nanoparticle translocation through polymer-brush-modified nanopores. *J. Phys. Condens. Matter*, 30:274006, 2018.

[60]Gabriel S. Longo and David H. Thompson. Ligand-receptor interactions between surfaces: The role of binary polymer spacers. *Langmuir*, 24:10324–10333, 2008.
[61]Mario Tagliazucchi, Yitzhak Rabin, and Igal Szleifer. Transport rectification in nanopores with outer membranes modified with surface charges and polyelectrolytes. *ACS Nano*, 7:9085–9097, 2013.
[62]Gervasio Zaldivar, Martin Conda-Sheridan, and Mario Tagliazucchi. Scission energies of surfactant wormlike micelles loaded with nonpolar additives. *J. Colloid Interf. Sci.*, 604:757–766, 2021.
[63]Mario Tagliazucchi, Mónica Olvera de la Cruz, and Igal Szleifer. Self-organization of grafted polyelectrolyte layers via the coupling of chemical equilibrium and physical interactions. *Proc. Natl. Acad. Sci.*, 107:5300–5305, 2010.
[64]Suman Chakraborty. Order parameter modeling of fluid dynamics in narrow confinements subjected to hydrophobic interactions. *Phys. Rev. Lett.*, 99:094504, 2007.
[65]Mario Tagliazucchi, Yitzhak Rabin, and Igal Szleifer. Ion transport and molecular organization are coupled in polyelectrolyte-modified nanopores. *J. Amer. Chem. Soc.*, 133:17753–17763, 2011.
[66]Oliver Weismantel, Aikaterini A. Galata, Morteza Sadeghi, Achim Kröger, and Martin Kröger. Efficient generation of self-avoiding, semiflexible rotational isomeric chain ensembles in bulk, in confined geometries, and on surfaces. *Comput. Phys. Commun.*, 270:108176, 2022.
[67]Tongchuan Suo and Mark D Whitmore. Doubly self-consistent field theory of grafted polymers under simple shear in steady state. *J. Chem. Phys.*, 140:114901, 2014.
[68]Morteza Sadeghi, Mohammad Hassan Saidi, Ali Moosavi, and Arman Sadeghi. Unsteady solute dispersion by electrokinetic flow in a polyelectrolyte layer-grafted rectangular microchannel with wall absorption. *J. Fluid Mech.*, 887:A13, 2020.
[69]Guang Chen and Siddhartha Das. Electroosmotic transport in polyelectrolyte-grafted nanochannels with ph-dependent charge density. *J. Appl. Phys.*, 117:185304, 2015.
[70]Shashishekar P. Adiga and Donald W. Brenner. Stimuli-responsive polymer brushes for flow control through nanopores. *J Funct Biomater*, 3:239–256, 2012.
[71]Shashishekar P. Adiga and Donald W. Brenner. Toward designing smart nanovalves: Modeling of flow control through nanopores via the helix-coil transition of grafted polypeptide chains. *Macromolecules*, 40:1342–1348, 2007.
[72]Prakash Goswami and Suman Chakraborty. Semi-analytical solutions for electroosmotic flows with interfacial slip in microchannels of complex cross-sectional shapes. *Microfluid. Nanofluid.*, 11:255–267, 2011.
[73]Barry W Ninham and V Adrian Parsegian. Electrostatic potential between surfaces bearing ionizable groups in ionic equilibrium with physiologic saline solution. *J. Theor. Biol.*, 31:405–428, 1971.
[74]Mario Tagliazucchi and Igal Szleifer. Stimuli-responsive polymers grafted to nanopores and other nano-curved surfaces: structure, chemical equilibrium and transport. *Soft Matter*, 8:7292–7305, 2012.
[75]A. M. Ricci, M. Tagliazucchi, and E. J. Calvo. Charge regulation in redox active monolayers embedded in proton exchanger surfaces. *Phys. Chem. Chem. Phys.*, 14:9988–9995, 2012.
[76]Junyi Zhai, Zengping Xing, Shuxiang Dong, Jiefang Li, and D. Viehland. Detection of pico-tesla magnetic fields using magneto-electric sensors at room temperature. *Appl. Phys. Lett.*, 88:062510, 2006.
[77]B. Reid, R. Nuccitelli, and M. Zhao. Non-invasive measurement of bioelectric currents with a vibrating probe. *Nat. Protocols*, 2:661–669, 2007.
[78]N. Haned and M. Missous. Nano-tesla magnetic field magnetometry using an ingaas–algaas–gaas 2deg hall sensor. *Sensors Actuators A*, 102:216–222, 2003.
[79]R. L. Fagaly. Superconducting quantum interference device instruments and applications. *Rev. Sci. Instr.*, 77:101101, 2006.
[80]Tsuyoshi Uchiyama, Kaneo Mohri, and Shinsuke Nakayama. Measurement of spontaneous oscillatory magnetic field of guinea-pig smooth muscle preparation using pico-tesla resolution amorphous wire magneto-impedance sensor. *IEEE Trans. Magn.*, 47:3070–3073, 2011.
[81]Quanliang Cao, Xiaotao Han, and Liang Li. Configurations and control of magnetic fields for manipulating magnetic particles in microfluidic applications: magnet systems and manipulation mechanisms. *Lab Chip*, 14:2762–2777, 2014.
[82]Jyh-Ping Hsu, Shu-Tuan Yang, Chih-Yuan Lin, and Shiojenn Tseng. Voltage-controlled ion transport and selectivity in a conical nanopore functionalized with ph-tunable polyelectrolyte brushes. *J. Colloid Interf. Sci.*, 537:496–504, 2019.
[83]Chih-Yuan Lin, Jyh-Ping Hsu, and Li-Hsien Yeh. Rectification of ionic current in nanopores functionalized with bipolar polyelectrolyte brushes. *Sensors Actuators B*, 258:1223–1229, 2018.
[84]P. Kaushik, Pranab Kumar Mondal, Pranab Kumar Kundu, and Somchai Wongwises. Rotating electroosmotic flow through a polyelectrolyte-grafted microchannel: An analytical solution. *Phys. Fluids*, 31:022009, 2019.
[85]Arman Sadeghi. Theoretical modeling of electroosmotic flow in soft microchannels: A variational approach applied to the rectangular geometry. *Phys. Fluids*, 30:032004, 2018.
[86]Guang Chen, Harnoor Singh Sachar, and Siddhartha Das. Efficient electrochemomechanical energy conversion in nanochannels grafted with end-charged polyelectrolyte brushes at medium and high salt concentration. *Soft Matter*, 14:5246–5255, 2018.
[87]Jiaxuan Zheng and Yongjun Jian. Electroosmotic thrusters in soft nanochannels for space propulsion. *Phys. Fluids*, 32:122005, 2020.
[88]Ruilin Zhang, Mingming Ding, Xiaozheng Duan, and Tongfei Shi. Electrohydrodynamic behavior of polyelectrolyte vesicle accompanied with ions in solution through a narrow pore induced by electric field. *Phys. Fluids*, 33:121901, 2021.

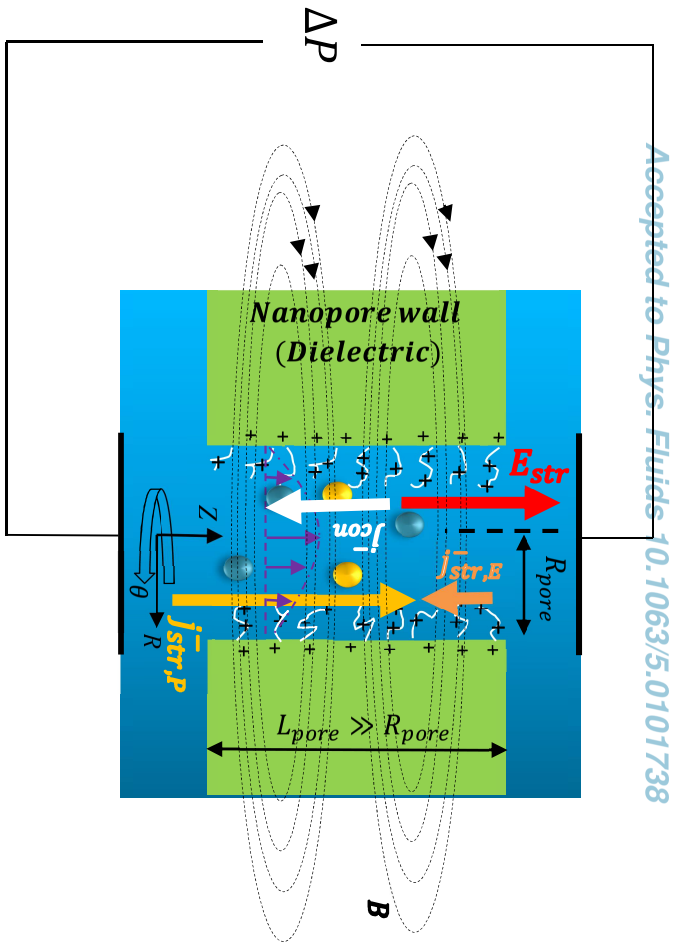

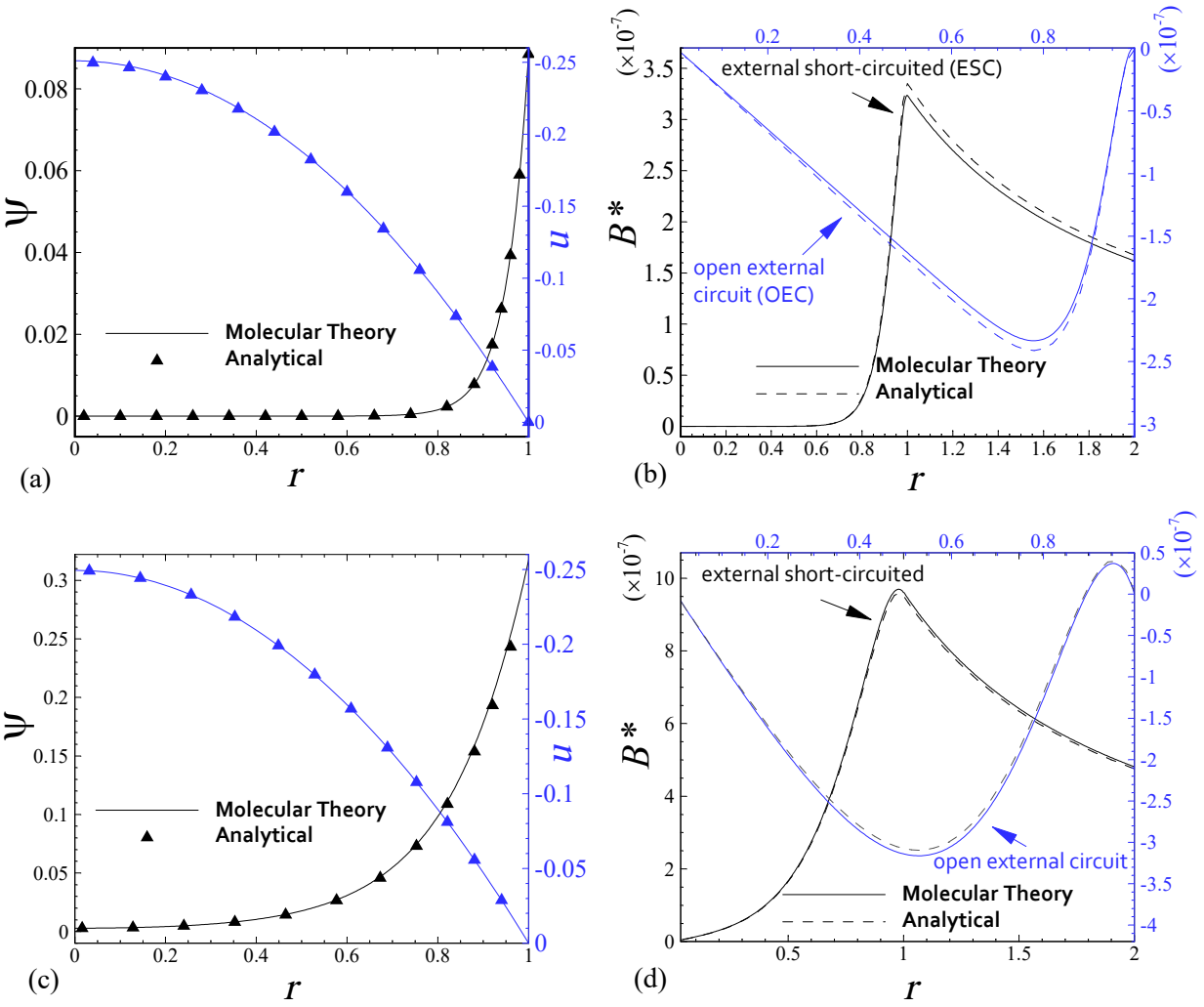

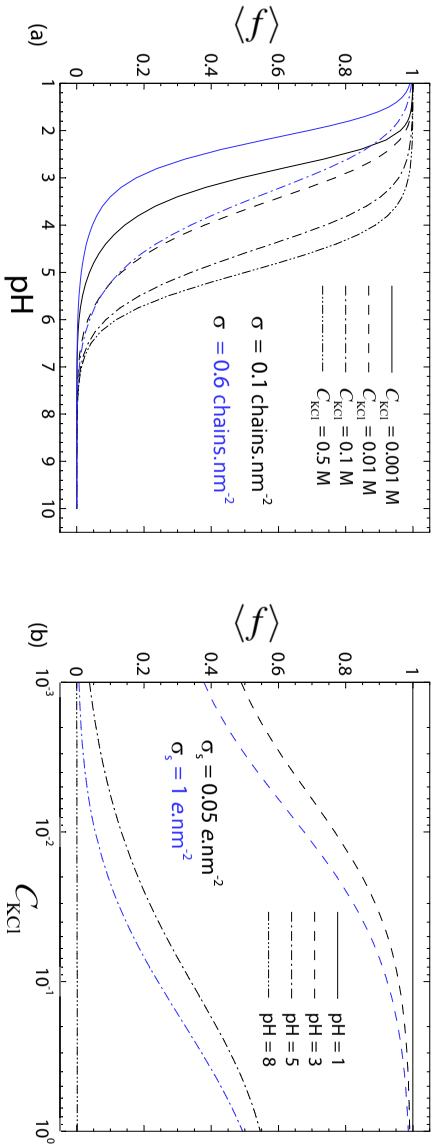

PLEASE CITE THIS ARTICLE AS DOI: 10.1063/5.0101738